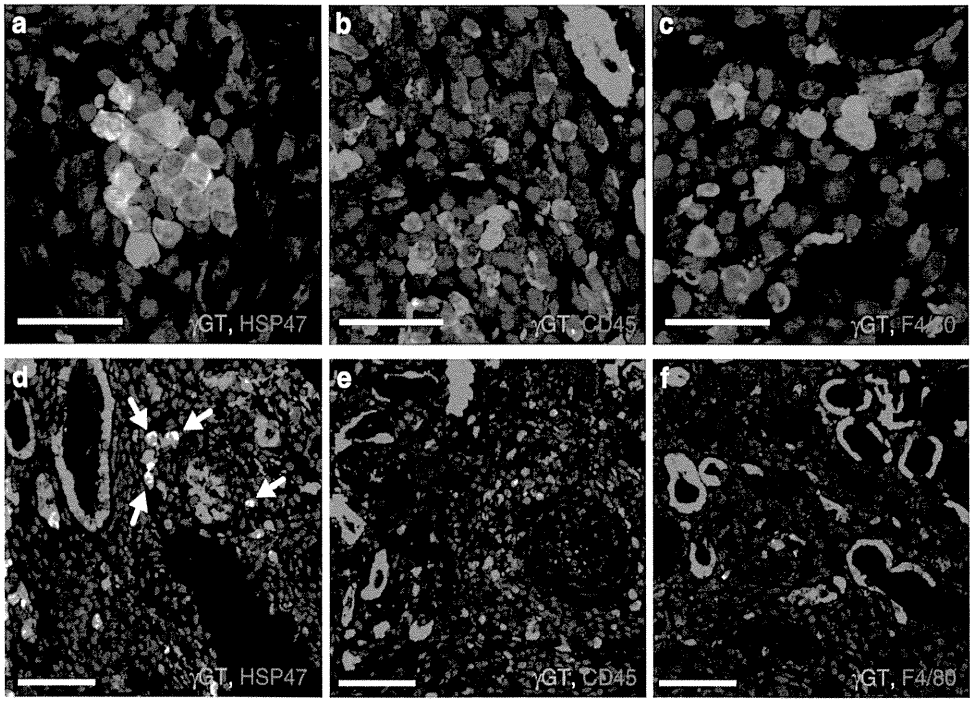

Figure 3 | Immunohistochemical characteristics of the epithelial-mesenchymal transition (EMT)-derived interstitial cells. (**a**–**f**) Immunostaining for HSP47 (**a**, **d**), CD45 (**b**, **e**), and F4/80 (**c**, **f**) in the kidneys of the unilateral ureteral obstruction (UUO) (SJL.γ-GT.Cre;EGFP double-transgenic) mice. A subpopulation of green interstitial cells expressed HSP47 (white arrows in **d**), a marker of collagen production. Scale bar = 25 μm in (**a**–**c**), 50 μm in (**d**–**f**).

functional data (proteinuria, serum creatinine, and so on) were not measured.

Immunohistochemistry

Formalin-fixed and paraffin-embedded kidney sections were prepared using standard procedures. With the exception of EGFP, a TSA kit (Molecular Probes/Invitrogen, Carlsbad, CA) was used to label primary antibodies with Alexa Fluor 555 (Molecular Probes). TO-PRO-3 (Molecular Probes) was used to detect nuclei. EGFP was detected using an anti-EGFP antibody followed by an Alexa Fluor 555–labeled secondary antibody.

The complete Materials and Methods are available online as Supplementary material.

DISCLOSURE

All the authors declared no competing interests.

ACKNOWLEDGMENTS

This work was supported in part by research grants from the Japanese Ministry of Education, Culture, Sports, Science and Technology and Asubio Pharma.

SUPPLEMENTARY MATERIAL

Table S1. Top 10 genes upregulated in the EMT-prone cultured cell lines only after co-stimulation with transforming growth factor-β1 and EGF for 24 hours.

Figure S1. Involvement of the EMT transcriptional regulators, Snail1 and HMGA2, in the EpH4 and MCT cells.

Figure S2. Quantitative analysis of the EMT-related-factors, Snail1 and HMGA2, using qRT-PCR.

Supplementary material is linked to the online version of the paper at http://www.nature.com/ki

REFERENCES

1. Iwano M, Plieth D, Danoff TM *et al.* Evidence that fibroblasts derive from epithelium during tissue fibrosis. *J Clin Invest* 2002; **110**: 341–350.
2. Zeisberg M, Neilson EG. Biomarkers for epithelial-mesenchymal transitions. *J Clin Invest* 2009; **119**: 1429–1437.
3. Quaggin SE, Kapus A. Scar wars: mapping the fate of epithelial-mesenchymal-myofibroblast transition. *Kidney Int* 2011; **80**: 41–50.
4. Inoue T, Okada H, Takenaka T *et al.* A case report suggesting the occurrence of epithelial-mesenchymal transition in obstructive nephropathy. *Clin Exp Nephrol* 2009; **13**: 385–388.
5. Humphreys BD, Lin SL, Kobayashi A *et al.* Fate tracing reveals the pericyte and not epithelial origin of myofibroblasts in kidney fibrosis. *Am J Pathol* 2010; **176**: 85–97.
6. Koesters R, Kaissling B, Lehir M *et al.* Tubular overexpression of transforming growth factor-beta1 induces autophagy and fibrosis but not mesenchymal transition of renal epithelial cells. *Am J Pathol* 2010; **177**: 632–643.
7. Lin SL, Kisseleva T, Brenner DA *et al.* Pericytes and perivascular fibroblasts are the primary source of collagen-producing cells in obstructive fibrosis of the kidney. *Am J Pathol* 2008; **173**: 1617–1627.
8. Brown KA, Aakre ME, Gorska AE *et al.* Induction by transforming growth factor-beta1 of epithelial to mesenchymal transition is a rare event *in vitro*. *Breast Cancer Res* 2004; **6**: R215–R231.
9. Inoue T, Okada H, Kobayashi T *et al.* Hepatocyte growth factor counteracts transforming growth factor-beta1, through attenuation of connective tissue growth factor induction, and prevents renal fibrogenesis in 5/6 nephrectomized mice. *FASEB J* 2003; **17**: 268–270.
10. Kato N, Watanabe Y, Ohno Y *et al.* Mapping quantitative trait loci for proteinuria-induced renal collagen deposition. *Kidney Int* 2008; **73**: 1017–1023.
11. Artunc F, Nasir O, Amann K *et al.* Serum- and glucocorticoid-inducible kinase 1 in doxorubicin-induced nephrotic syndrome. *Am J Physiol Renal Physiol* 2008; **295**: F1624–F1634.
12. Ma LJ, Fogo AB. Model of robust induction of glomerulosclerosis in mice: importance of genetic background. *Kidney Int* 2003; **64**: 350–355.
13. Zeisberg M, Yang C, Martino M *et al.* Fibroblasts derive from hepatocytes in liver fibrosis via epithelial to mesenchymal transition. *J Biol Chem* 2007; **282**: 23337–23347.

14. Kim J, Seok YM, Jung KJ *et al.* Reactive oxygen species/oxidative stress contributes to progression of kidney fibrosis following transient ischemic injury in mice. *Am J Physiol Renal Physiol* 2009; **297**: F461–F470.
15. Zeisberg EM, Tarnavski O, Zeisberg M *et al.* Endothelial-to-mesenchymal transition contributes to cardiac fibrosis. *Nat Med* 2007; **13**: 952–961.
16. Inoue T, Plieth D, Venkov CD *et al.* Antibodies against macrophages that overlap in specificity with fibroblasts. *Kidney Int* 2005; **67**: 2488–2493.
17. Bucala R, Spiegel LA, Chesney J *et al.* Circulating fibrocytes define a new leukocyte subpopulation that mediates tissue repair. *Mol Med* 1994; **1**: 71–81.
18. Sakai N, Wada T, Yokoyama H *et al.* Secondary lymphoid tissue chemokine (SLC/CCL21)/CCR7 signaling regulates fibrocytes in renal fibrosis. *Proc Natl Acad Sci USA* 2006; **103**: 14098–14103.
19. Okada H, Inoue T, Kikuta T *et al.* Poly(ADP-ribose) polymerase-1 enhances transcription of the profibrotic CCN2 gene. *J Am Soc Nephrol* 2008; **19**: 933–942.
20. Okada H, Inoue T, Kikuta T *et al.* A possible anti-inflammatory role of angiotensin II type 2 receptor in immune-mediated glomerulonephritis during type 1 receptor blockade. *Am J Pathol* 2006; **169**: 1577–1589.

A calcium-dependent protease as a potential therapeutic target for Wolfram syndrome

Simin Lu[a,b], Kohsuke Kanekura[a], Takashi Hara[a], Jana Mahadevan[a], Larry D. Spears[a], Christine M. Oslowski[c], Rita Martinez[d], Mayu Yamazaki-Inoue[e], Masashi Toyoda[e], Amber Neilson[d], Patrick Blanner[d], Cris M. Brown[a], Clay F. Semenkovich[a], Bess A. Marshall[f], Tamara Hershey[g], Akihiro Umezawa[e], Peter A. Greer[h], and Fumihiko Urano[a,i,1]

[a]Department of Medicine, Division of Endocrinology, Metabolism, and Lipid Research, Washington University School of Medicine, St. Louis, MO 63110; [b]Graduate School of Biomedical Sciences, University of Massachusetts Medical School, Worcester, MA 01655; [c]Department of Medicine, Boston University School of Medicine, Boston, MA 02118; [d]Department of Genetics, iPSC core facility, Washington University School of Medicine, St. Louis, MO 63110; [e]Department of Reproductive Biology, National Center for Child Health and Development, Tokyo 157-8535, Japan; [f]Department of Pediatrics, Washington University School of Medicine, St. Louis, MO 63110; [g]Departments of Psychiatry, Neurology, and Radiology, Washington University School of Medicine, St. Louis, MO 63110; [h]Department of Pathology and Molecular Medicine, Queen's University, Division of Cancer Biology and Genetics, Queen's Cancer Research Institute, Kingston, Ontario K7L3N6, Canada; and [i]Department of Pathology and Immunology, Washington University School of Medicine, St. Louis, MO 63110

Edited by Stephen O'Rahilly, University of Cambridge, Cambridge, United Kingdom, and approved November 7, 2014 (received for review November 4, 2014)

Wolfram syndrome is a genetic disorder characterized by diabetes and neurodegeneration and considered as an endoplasmic reticulum (ER) disease. Despite the underlying importance of ER dysfunction in Wolfram syndrome and the identification of two causative genes, Wolfram syndrome 1 (*WFS1*) and Wolfram syndrome 2 (*WFS2*), a molecular mechanism linking the ER to death of neurons and β cells has not been elucidated. Here we implicate calpain 2 in the mechanism of cell death in Wolfram syndrome. Calpain 2 is negatively regulated by WFS2, and elevated activation of calpain 2 by WFS2-knockdown correlates with cell death. Calpain activation is also induced by high cytosolic calcium mediated by the loss of function of WFS1. Calpain hyperactivation is observed in the WFS1 knockout mouse as well as in neural progenitor cells derived from induced pluripotent stem (iPS) cells of Wolfram syndrome patients. A small-scale small-molecule screen targeting ER calcium homeostasis reveals that dantrolene can prevent cell death in neural progenitor cells derived from Wolfram syndrome iPS cells. Our results demonstrate that calpain and the pathway leading its activation provides potential therapeutic targets for Wolfram syndrome and other ER diseases.

Wolfram syndrome | endoplasmic reticulum | diabetes | neurodegeneration | treatment

The endoplasmic reticulum (ER) takes center stage for protein production, redox regulation, calcium homeostasis, and cell death (1, 2). It follows that genetic or acquired ER dysfunction can trigger a variety of common diseases, including neurodegenerative diseases, metabolic disorders, and inflammatory bowel disease (3, 4). Breakdown in ER function is also associated with genetic disorders such as Wolfram syndrome (5–8). It is challenging to determine the exact effects of ER dysfunction on the fate of affected cells in common diseases with polygenic and multifactorial etiologies. In contrast, we reasoned that it should be possible to define the role of ER dysfunction in mechanistically homogenous patient populations, especially in rare diseases with a monogenic basis, such as Wolfram syndrome (9).

Wolfram syndrome (OMIM 222300) is a rare autosomal recessive disorder characterized by juvenile-onset diabetes mellitus and bilateral optic atrophy (7). Insulin-dependent diabetes usually occurs as the initial manifestation during the first decade of life, whereas the diagnosis of Wolfram syndrome is invariably later, with onset of symptoms in the second and ensuing decades (7, 10, 11). Two causative genes for this genetic disorder have been identified and named Wolfram syndrome 1 (*WFS1*) and Wolfram syndrome 2 (*WFS2*) (12, 13). It has been shown that multiple mutations in the *WFS1* gene, as well as a specific mutation in the *WFS2* gene, lead to β cell death and neurodegeneration through ER and mitochondrial dysfunction (5, 6, 14–16). *WFS1* gene variants are also associated with a risk of type 2 diabetes (17). Moreover, a specific *WFS1* variant can cause autosomal dominant diabetes (18), raising the possibility that this rare disorder is relevant to common molecular mechanisms altered in diabetes and other human chronic diseases in which ER dysfunction is involved.

Despite the underlying importance of ER malfunction in Wolfram syndrome, and the identification of *WFS1* and *WFS2* genes, a molecular mechanism linking the ER to death of neurons and β cells has not been elucidated. Here we show that the calpain protease provides a mechanistic link between the ER and death of neurons and β cells in Wolfram syndrome.

Results

The causative genes for Wolfram syndrome, *WFS1* and *WFS2*, encode transmembrane proteins localized to the ER (5, 12, 13). Mutations in the *WFS1* or *WFS2* have been shown to induce neuronal and β cell death. To determine the cell death pathways emanating from the ER, we sought proteins associated with Wolfram syndrome causative gene products. HEK293 cells were transfected with a GST-tagged WFS2 expression plasmid. The GST-WFS2 protein was purified along with associated proteins on a glutathione affinity resin. These proteins were separated by

Significance

Wolfram syndrome is an autosomal recessive disorder characterized by juvenile diabetes and neurodegeneration, and is considered a prototype of human endoplasmic reticulum (ER) disease. Wolfram syndrome is caused by loss of function mutations of Wolfram syndrome 1 or Wolfram syndrome 2 genes, which encode transmembrane proteins localized to the ER. Despite its rarity, Wolfram syndrome represents the best human disease model currently available to identify drugs and biomarkers associated with ER health. Furthermore, this syndrome is ideal for studying the mechanisms of ER stress-mediated death of neurons and β cells. Here we report that the pathway leading to calpain activation offers potential drug targets for Wolfram syndrome and substrates for calpain might serve as biomarkers for this syndrome.

Author contributions: S.L., P.A.G., and F.U. designed research; S.L., K.K., T. Hara, J.M., L.D.S., C.M.O., R.M., M.Y.-I., M.T., A.N., P.B., and C.M.B. performed research; S.L., B.A.M., T. Hershey, A.U., and F.U. contributed new reagents/analytic tools; S.L., K.K., T. Hara, J.M., L.D.S., C.M.O., R.M., M.Y.-I., M.T., A.N., P.B., C.M.B., C.F.S., P.A.G., and F.U. analyzed data; and S.L., C.F.S., P.A.G., and F.U. wrote the paper.

The authors declare no conflict of interest.

This article is a PNAS Direct Submission.

Freely available online through the PNAS open access option.

[1]To whom correspondence should be addressed. Email: urano@dom.wustl.edu.

This article contains supporting information online at www.pnas.org/lookup/suppl/doi:10.1073/pnas.1421055111/-/DCSupplemental.

SDS/PAGE and visualized by Coomassie staining. Matrix-assisted laser desorption/ionization-time of flight (MALDI-TOF) mass spectroscopic analysis revealed 13 interacting proteins (Table S1), and one of the WFS2-associated polypeptides was CAPN2, the catalytic subunit of calpain 2, a member of the calcium dependent cysteine proteases family whose members mediate diverse biological functions including cell death (19–21) (Fig. 1*A*). Previous studies have shown that calpain 2 activation is regulated on the ER membrane and it plays a role in ER stress-induced apoptosis and β cell death (20, 22–24), which prompted us to study the role of WFS2 in calpain 2 activation.

Calpain 2 is a heterodimer consisting the CAPN2 catalytic subunit and the CAPNS1 (previously known as CAPN4) regulatory subunit. We first verified that WFS2 interacts with calpain 2 by showing that endogenous calpain 2 subunits CAPN2 (Fig. 1*B*) and CAPNS1 (Fig. 1*C*) each associated with GST-tagged WFS2 expressed in HEK293 cells. Endogenous CAPN2 was also found to be coimmunoprecipated with N- or C-terminal FLAG-tagged WFS2 expressed in HEK293 cells (Fig. S1 *A* and *B*, respectively). To further confirm these findings, we performed a coimmunoprecipitation experiment in Neuro2a cells (a mouse neuroblastoma cell line) and INS-1 832/13 cells (a rat pancreatic β cell line)

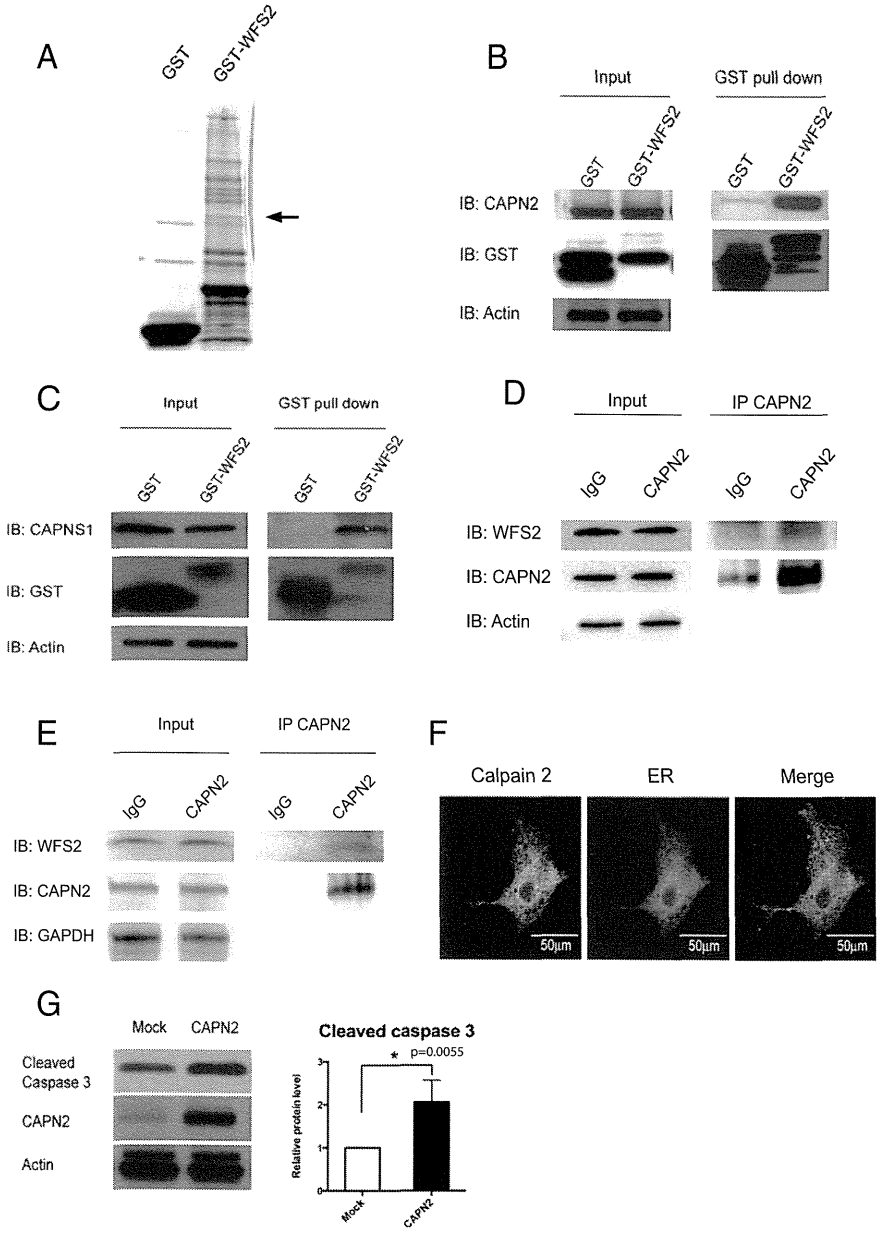

Fig. 1. WFS2 interacts with CAPN2. (*A*) Affinity purification of WFS2-associated proteins from HEK293 cells transfected with GST or GST-WFS2 expression plasmid. Proteins were separated by SDS/PAGE and visualized by Coomassie blue staining. CAPN2 was identified by MALDI-TOF analysis and denoted by an arrow. (*B*) GST-tagged WFS2 was pulled down on a glutathione affinity resin from lysates of HEK293 cells transfected with a GST-WFS2 expression plasmid, and the pulled-down products were analyzed for CAPN2 by immunoblotting with anti-CAPN2 antibody. (*C*) GST-tagged WFS2 was pulled down on a glutathione affinity resin from lysates of HEK293 cells transfected with GST-WFS2 expression plasmid and the pulled-down products were analyzed for CAPNS1 by immunoblotting with anti-CAPNS1 antibody. (*D*) Lysates of Neuro2a cells were immunoprecipitated with IgG or anti-calpain 2 antibodies. Lysates of IgG and anti-calpain 2 immunoprecipitates were analyzed for WFS2, CAPN2 or actin by immunoblotting. (*E*) Lysates of INS-1 832/13 cells were immunoprecipitated with IgG or anti-calpain 2 antibody. Lysates of IgG and anti-calpain 2 immunoprecipitates were analyzed for WFS2, CAPN2 or actin by immunoblotting. (*F*) COS7 cells were transfected with pDsRed2-ER vector (*Center*) and stained with anti-calpain 2 antibody (*Left*). (*Right*) A merged image is shown. (*G*) HEK293 cells were transfected with empty expression plasmid or a CAPN2 expression plasmid. Apoptosis was monitored by immunoblotting analysis of caspase 3 cleavage. (*Left*) Expression levels of CAPN2 and actin were measured by immunoblotting. (*Right*) Quantification of immunoblot is shown ($n = 3$, $^*P < 0.05$).

and found that endogenous WFS2 interacted with endogenous CAPN2 (Fig. 1 *D* and *E*). WFS2 is known to be a transmembrane protein localized to the ER. We therefore explored the possibility that calpain 2 might also localize to the ER. We transfected COS7 cells with pDsRed2-ER vector to visualize ER. Immunofluorescence staining of COS7 cells showed that endogenous calpain 2 was mainly localized to the cytosol, but also showed that a small portion colocalized with DsRed2-ER protein at the ER (Fig. 1*F*). Cell fractionation followed by immunoblot further confirmed this observation (Fig. S1*C*). Collectively, these results suggest that calpain 2 interacts with WFS2 at the cytosolic face of the ER.

Calpain hyperactivation has been shown to contribute to cell loss in various diseases (19), raising the possibility that calpain 2 might be involved in the regulation of cell death. To verify this issue, we overexpressed CAPN2, the catalytic subunit of calpain 2, and observed increase of cleaved caspase-3 in HEK293 cells indicating that hyperactivation of calpain 2 induces cell death (Fig. 1*G*).

To determine whether WFS2 plays a role in cell survival, we suppressed WFS2 expression in mouse neuronal NSC34 cells using siRNA and measured cell death under normal and ER stress conditions. WFS2 knockdown was associated with increased cleavage of caspase-3 in normal or ER stressed conditions (Fig. 2 *A* and *B*). We subsequently evaluated calpain 2 activation by measuring the cleavage of alpha II spectrin, a substrate for calpain 2. RNAi-mediated knockdown of WFS2 induced calpain activation, especially under ER stress conditions (Fig. 2*A*).

In patients with Wolfram syndrome, destruction of β cells leads to juvenile-onset diabetes (25). This finding prompted us to examine whether WFS2 was also involved in pancreatic β cell death. As was seen in neuronal cells, knockdown of WFS2 in rodent β cell lines INS1 832/13 (Fig. 2*C*) and MIN6 (Fig. S2) was also associated with increased caspase-3 cleavage under both normal and ER stress conditions. The association of WFS2 with calpain 2 and their involvement in cell viability suggested that calpain 2 activation might be the cause of cell death in WFS2-deficient cells. To further explore the relationship between WFS2 and calpain 2, we expressed WFS2 together with the calpain 2 catalytic subunit CAPN2 and measured apoptosis. Ectopic expression of WFS2 significantly suppressed calpain 2-associated apoptosis under normal and ER stress conditions (Fig. 2*D*, lane 4 and lane 8, and Fig. 2*E*). Next, we tested whether CAPN2 mediates cell death induced by WFS2 deficiency. When CAPN2 was silenced in WFS2-deficient cells, apoptosis was partially suppressed compared with untreated WFS2-deficient cells (Fig. 2*F*). Taken together, these results suggest that WFS2 is a negative regulator of calpain 2 proapoptotic functions.

To further confirm that loss of function of WFS2 leads to cell death mediated by calpain 2, we tested if calpeptin, a calpain inhibitor, could prevent cell death in WFS2-deficient cells. In agreement with previous observations, calpeptin treatment prevented WFS2-knockdown-mediated cell death in neuronal (Fig. 3 *A* and *B*) and β cell lines (Fig. 3*C* and Fig. S3*A*). Collectively, these results indicate that WFS2 is a suppressor of calpain 2-mediated cell death.

CAPN2 is the catalytic subunit of calpain 2. CAPN2 forms a heterodimer with the regulatory subunit, CAPNS1, which is required for protease activity and stability. We next explored the role of WFS2 in CAPN2 and CAPNS1 protein stability. Ectopic expression or RNAi-mediated knockdown of WFS2 did not correlate with changes in the steady-state expression of CAPN2 (Fig. S3*B*). By contrast, overexpression of WFS2 significantly reduced CAPNS1 protein expression (Fig. 3*D*) and transient suppression of WFS2 slightly increased CAPNS1 protein expression (Fig. 3*D*). These data suggest that WFS2 might be involved in CAPNS1 protein turnover, which is supported by the data showing that GST-tagged WFS2 expressed in HEK293 cells associated with endogenous CAPNS1 (Fig. 1*C*). To investigate whether WFS2 regulates CAPNS1 stability through the ubiquitin-proteasome pathway, we treated HEK293 cells ectopically expressing WFS2 with a proteasome inhibitor, MG132, and then measured CAPNS1 protein level. MG132 treatment stabilized CAPNS1 protein in cells ectopically expressing WFS2 (Fig. 3*E*). Furthermore, we performed cycloheximide chase experiments using HEK293 cells ectopically expressing WFS2 and quantified CAPNS1 protein levels at different time points. Ectopic expression of WFS2 was associated with significantly accelerated CAPNS1 protein loss, indicating that WFS2 contributes to posttranslational regulation of CAPNS1 (Fig. 3*F*). To further assess whether WFS2 is involved in the ubiquitination of CAPNS1, we measured the levels of CAPNS1 ubiquitination in cells ectopically expressing WFS2 and observed that CAPNS1 ubiquitination was increased by ectopic expression of WFS2 (Fig. 3*G*).

To further investigate the role of WFS2 in calpain 2 regulation, we collected brain lysates from WFS2 knockout mice. Measured levels of cleaved spectrin, a well characterized substrate for calpain (26). Notably, protein expression levels of cleaved spectrin, as well as CAPNS1, were significantly increased in WFS2 knockout mice compared with control mice (Fig. 3*H*). Collectively, these results indicate that WFS2 inhibits calpain 2 activation by regulating CAPNS1 degradation mediated by the ubiquitin-proteasome system.

Calpain 2 is a calcium-dependent protease. *WFS1*, the other causative gene for Wolfram syndrome, has been shown to be involved in calcium homeostasis (27, 28), suggesting that the loss of function of WFS1 may also cause calpain activation. To evaluate this possibility, we measured calpain activation levels in brain tissues from WFS1 brain-specific knockout and control mice. We observed a significant increase in a calpain-specific spectrin cleavage product, reflecting higher calpain activation levels in WFS1 knockout mice compared with control mice (Fig. 4*A*). The suppression levels of WFS1 in different parts of the brain were shown in Fig. 4*B*. To further confirm that calpain is activated by the loss of WFS1, we looked for other calpain substrates in brain tissues from WFS1 knockout mice using a proteomics approach. Two-dimensional fluorescence gel electrophoresis identified 12 proteins differentially expressed between cerebellums of WFS1 knockout mice and those of control mice (Fig. 4 *C* and *D*). Among these, myelin basic protein (MBP) is a known substrate for calpain in the brain (29). We measured myelin basic protein levels in brain lysates from WFS1 knockout and control mice. Indeed, the cleavage and degradation of myelin basic protein was increased in WFS1 knockout mice relative to control mice (Fig. 4*E*).

Next, we looked for evidence of increased calpain activity in Wolfram syndrome patient cells. We created neural progenitor cells derived from induced pluripotent stem cells (iPSCs) of Wolfram syndrome patients with mutations in *WFS1*. Fibroblasts from four unaffected controls and five patients with Wolfram syndrome were transduced with four reprogramming genes (Sox2, Oct4, c-Myc, and Klf4) (30) (Table S2). We produced at least 10 iPSC clones from each control and Wolfram patient. All control- and Wolfram-iPSCs, exhibited characteristic human embryonic stem cell morphology, expressed pluripotency markers including ALP, NANOG, SOX2, SSEA4, TRA-1–81, and had a normal karyotype (Fig. 5 *A–F*). To create neural progenitor cells, we first formed neural aggregates from iPSCs. Neural aggregates were harvested at day 5, replated onto new plates to give rise to colonies containing neural rosette structures. At day 12, neural rosette clusters were collected, replated, and used as neural progenitor cells. Consistent with the data from WFS1 and WFS2 knockout mice, we observed that spectrin cleavage was increased in neural progenitor cells derived from Wolfram-iPSCs relative to control iPSCs, which indicates increased calpain activity (Fig. 5*G*).

Because calpain is known to be activated by high calcium, we explored the possibility that cytoplasmic calcium may be increased in patient cells by staining neural progenitor cells derived from

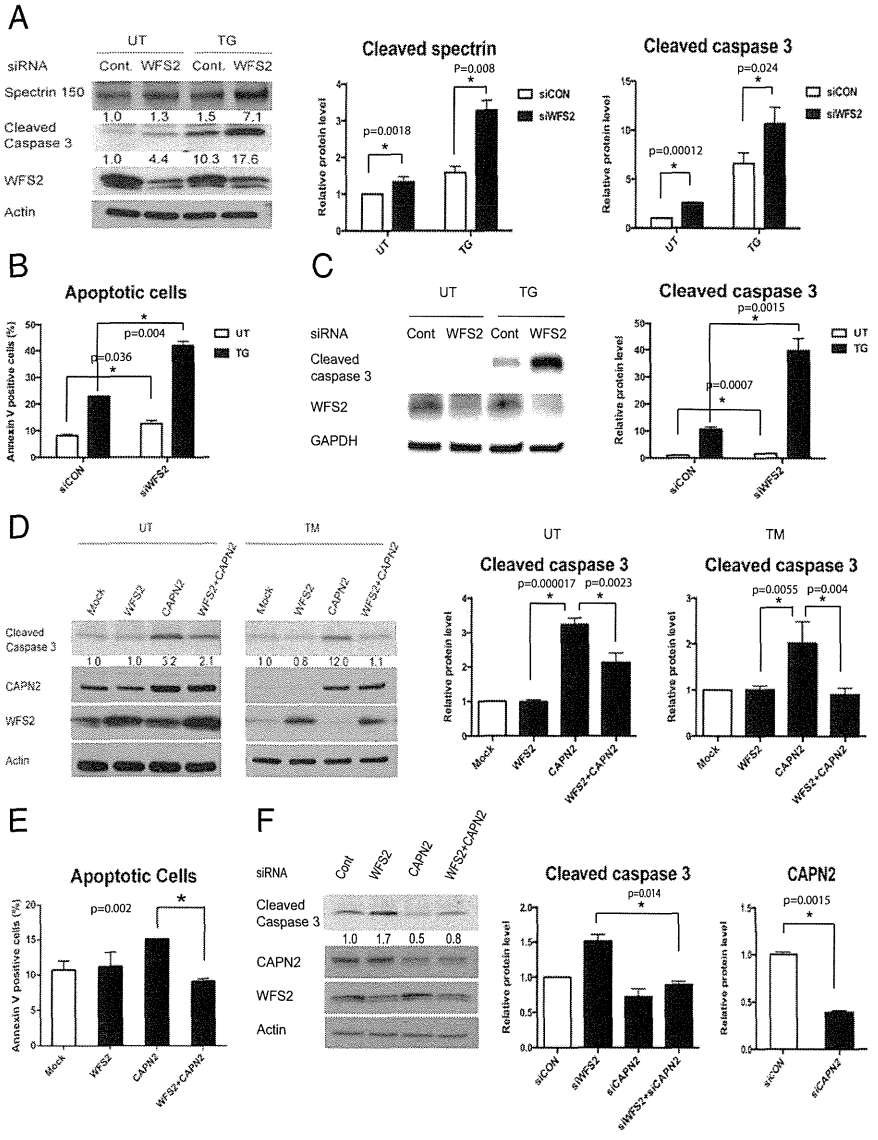

Fig. 2. WFS2 suppresses cell death mediated by CAPN2. (*A*) NSC34 cells were transfected with control scrambled siRNA or siRNA directed against WFS2, and then treated with 0.5μM thapsigargin (TG) for 6 h or untreated (UT). Apoptosis was monitored by immunoblotting analysis of cleaved caspase 3. (*Left*) Protein levels of cleaved spectrin, WFS2, and actin were measured by immunoblotting. (*Right*) Quantifications of cleaved spectrin and cleaved caspase 3 are shown ($n = 5$, $^*P < 0.05$). (*B*) NSC34 cells were transfected with control scrambled siRNA or siRNA directed against WFS2, and then treated with 0.5 μM thapsigargin (TG) for 6 h or untreated (UT). Apoptosis was monitored by Annexin V staining followed by flow cytometry analysis. ($n = 3$, $^*P < 0.05$). (*C*) INS-1 832/13 cells were transfected with control scrambled siRNA or siRNA directed against WFS2, and then treated with 0.5 μM thapsigargin (TG) for 6 h or untreated (UT). (*Left*) Expression levels of cleaved caspase 3, WFS2, and actin were measured by immunoblotting. (*Right*) Protein levels of cleaved caspase 3 are quantified ($n = 3$, $^*P < 0.05$). (*D*) NSC34 cells were transfected with empty expression plasmid (Mock), WFS2 expression plasmid, CAPN2 expression plasmid or cotransfected with WFS1 and CAPN2 expression plasmids. Twenty-four h post transfection, cells were treated with 5 μg/mL tunicamycin (TM) for 16 h or untreated (UT). Apoptosis was monitored by immunoblotting analysis of the relative levels of cleaved caspase 3 (indicated in *Left*). Expression levels of CAPN2, WFS2, and actin were also measured by immunoblotting. Quantification of cleaved caspase 3 levels under untreated (*Center*) and tunicamycin treated (*Right*) conditions are shown as bar graphs. ($n = 5$, $^*P < 0.05$). (*E*) Neuro2a cells transfected with empty expression plasmid (Mock), WFS2 expression plasmid, CAPN2 expression plasmid or cotransfected with WFS1 and CAPN2 expression plasmids were examined for apoptosis by Annexin V staining followed by flow cytometry analysis (*Right*, $n = 3$, $^*P < 0.05$). (*F*) NSC34 cells were transfected with scrambled siRNA (Cont), WFS2 siRNA, CAPN2 siRNA or cotransfected with WFS2 siRNA and CAPN2 siRNA. Apoptosis was detected by immunoblotting of cleaved caspase 3. (*Left*) Protein levels of CAPN2, WFS2 and actin were also shown. (*Right*) Quantification of immunoblotting is shown ($n = 3$, $^*P < 0.05$).

control- and Wolfram-iPSCs with Fura-2, a fluorescent calcium indicator which enables accurate measurements of cytoplasmic calcium concentrations. Fig. 5*H*, *Left*, shows that cytoplasmic calcium levels were higher in Wolfram-iPSC-derived neuronal cells relative to control cells. This result was confirmed by staining these cells with another fluorescent calcium indicator, Fluo-4 (Fig. 5*H*, *Right*). Collectively, these results indicate that loss of function of WFS1 increases cytoplasmic calcium levels, leading to calpain activation.

The results shown above argue that the pathway leading to calpain activation provides potential therapeutic targets for Wolfram syndrome. To test this concept, we elected to focus on modulating cytosolic calcium and performed a small-scale screen to identify chemical compounds that could prevent cell death mediated by thapsigargin, a known inhibitor for ER calcium ATPase. Among 73 well characterized chemical compounds that we tested (Table S3), 8 could significantly suppress thapsigargin-mediated cell death. These were PARP inhibitor, dantrolene, NS398, pioglitazone, calpain inhibitor III, docosahexaenoic acid (DHA), rapamycin, and GLP-1 (Fig. 6*A*). GLP-1, pioglitazone, and rapamycin are FDA-approved drugs and have been shown to confer protection against ER stress-mediated cell death (27, 31–33). Dantrolene is another FDA-approved drug clinically used for muscle spasticity and malignant hyperthermia (34). Previous studies

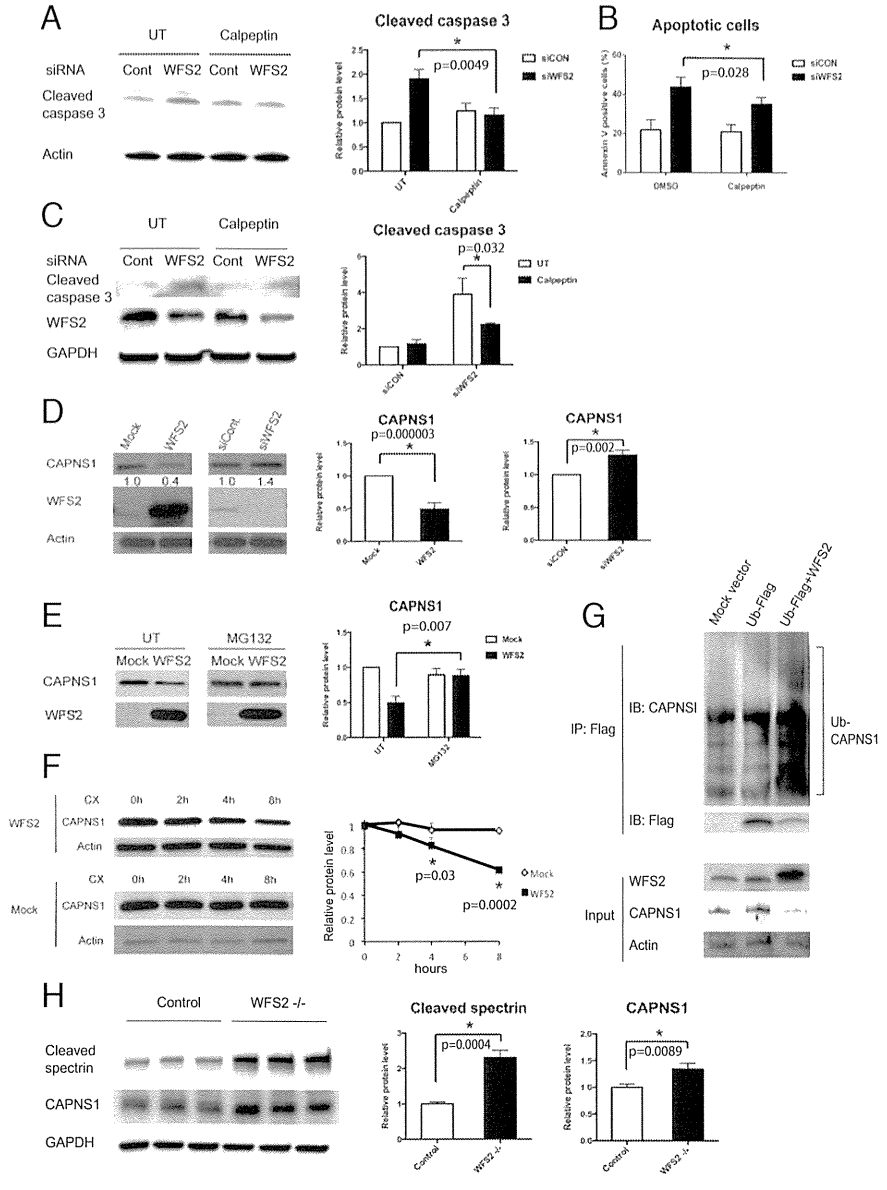

Fig. 3. WFS2 regulates calpain activity through CAPNS1. (*A*) Neuro-2a cells were transfected with siRNA against WFS2 or a control scrambled siRNA. Thirty-six h after transfection, cells were treated with or without 100μM calpeptin for 12 h. Cleaved caspase 3 and actin levels were assessed by immunoblotting (left panel). Cleaved caspase 3 protein levels are quantified in the right panel ($n = 3$, $^*P < 0.05$). (*B*) Neuro-2a cells were transfected with siRNA against WFS2 or scrambled siRNA. Thirty-six h after transfection, cells were treated with or without 100 μM calpeptin for 12 h. Early stage apoptosis was monitored by Annexin V staining followed by flow cytometry ($n = 3$, $^*P < 0.05$). (*C*) INS-1 832/13 cells were transfected with scrambled siRNA and WFS2 siRNA. Twenty-four h after transfection, cells were treated with or without 5 μM calpeptin for 24 h. Cleaved caspase 3, WFS2 and actin levels were monitored by immunoblotting (*Left*) and quantified (*Right*) ($n = 3$, $^*P < 0.05$). (*D*, *Left*) CAPNS1, WFS2, and actin levels were assessed by immunoblotting in HEK293 cells transfected with empty expression plasmid (Mock), WFS2 expression plasmid, scrambled siRNA (siCON), or WFS2 siRNA (siWFS2). (*D*, *Right*) Protein levels of CAPNS1 are quantified ($n = 5$, $^*P < 0.05$). (*E*) HEK293 cells were transfected with empty (Mock) or WFS2 expression plasmid, and then treated with MG132 (2 μM) or untreated (UT). Expression levels of CAPNS1 and WFS2 were measured by immunoblotting (*Left*) and quantified (*Right*) ($n = 4$, $^*P < 0.05$). (*F*) HEK293 cells were transfected with empty or WFS2 expression plasmid, and then treated with cycloheximide (100 μM) for indicated times. (*Left*) Expression levels of CAPNS1 and actin were measured by immunoblotting. (*Right*) Band intensities corresponding to CAPNS1 in *Left* were quantified by Image J and plotted as relative rates of the signals at 0 h ($n = 3$, $^*P < 0.05$). (*G*) NSC34 cells were transfected with mock empty vector, FLAG tagged ubiquitin (Ub-FLAG) plasmid or cotransfected with WFS2 expression plasmid and Ub-FLAG plasmid. Cell lysates were immunoprecipitated with FLAG affinity beads and analyzed for ubiquitin conjugated proteins by immunoblotting. Levels of CAPNS1 and Ub-FLAG protein were measured in the precipitates. WFS2, CAPNS1 and actin expression was monitored in the input samples. (*H*) Brain lysates from control and WFS2 knockout mice were analyzed by immunoblotting. Protein levels of cleaved spectrin and CAPNS1 were determined (*Left*) and quantified (*Center* and *Right*) (each group $n = 3$, $^*P < 0.05$).

have shown that dantrolene is an inhibitor of the ER-localized ryanodine receptors and suppresses leakage of calcium from the ER to cytosol (35, 36). We thus hypothesized that dantrolene could confer protection against cell death in Wolfram syndrome, and performed a series of experiments to investigate this possibility. We first examined whether dantrolene could decrease cytoplasmic calcium levels. As expected, dantrolene treatment decreased cytosolic calcium levels in INS-1 832/13 and NSC34 cells (Fig. S4 *A* and *B*). We next asked whether dantrolene could restore cytosolic calcium levels in WFS1-deficient cells. RNAi-mediated WFS1 knockdown increased cytosolic calcium levels relative to control cells, and dantrolene treatment restored cytosolic calcium levels in WFS1-knockdown INS-1 832/13 cells (Fig. 6*B*, *Left*) as well as WFS1-knockdown NSC34 cells (Fig. 6*B*, *Right*). Next, to determine whether dantrolene confered protection in WFS1-deficient cells, we treated WFS1 silenced INS-1 832/13 cells with dantrolene and observed suppression of apoptosis (Fig. 6*C*) and calpain activity (Fig. 6*D*). Dantrolene treatment also prevented

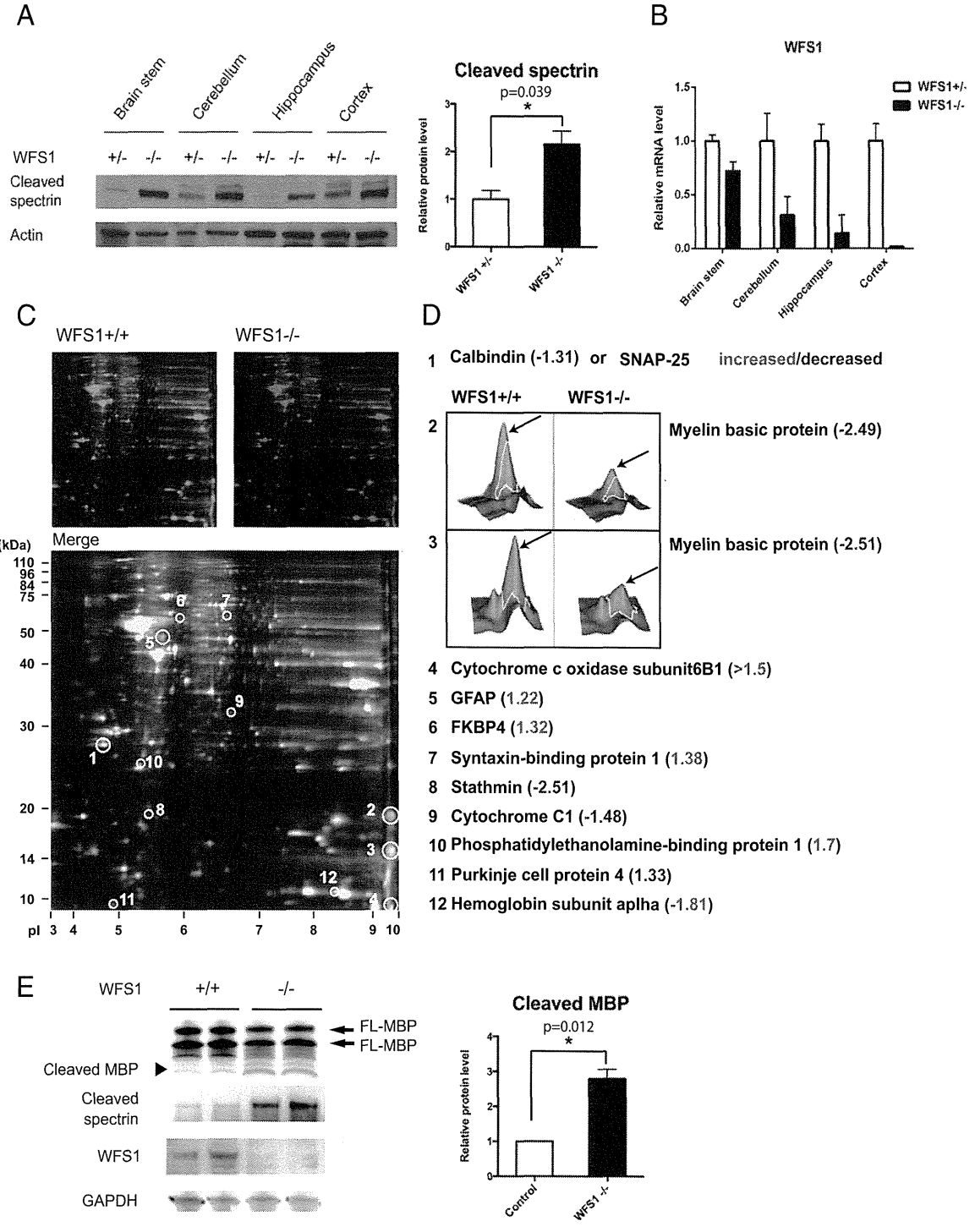

Fig. 4. Evidence of Calpain 2 activation in a mouse model of Wolfram syndrome. (*A*) Protein was extracted from brain tissues of WFS1 brain-specific knockout (–/–) and control (+/–) mice. (*Left*) Cleaved alpha II spectrin and actin levels were determined by immunoblot analysis. (*Right*) Quantification of cleaved spectrin is shown (each group $n = 10$, $^*P < 0.05$). (*B*) WFS1 mRNA levels in different parts of brain in WFS1$^{-/-}$ and WFS1$^{+/-}$ mice were measured by qRT-PCR. (*C*) Two-dimensional fluorescence difference gel electrophoresis of cerebellum proteins from WFS1 knockout (WFS1$^{-/-}$, labeled in red) and control (WFS1$^{+/+}$, labeled in green) mice showing common (Merge, labeled in yellow) and unique proteins (circled). (*D*) The protein expression ratios between WFS1 knockout and control mice were generated, and differentially expressed spots were analyzed by MALDI-TOF mass spectrometry. Quantitative diagrams of spots #2 and #3, identified by mass spectrometry as myelin basic protein, showing lower levels of expression in WFS1 knockout mice compared with control mice. (*E*) Protein was extracted from cerebellums of WFS1 brain-specific knockout (–/–) and control (+/+) mice. Cleaved myelin basic protein (black arrow), cleaved spectrin, WFS1 and GAPDH levels were determined by immunoblot analysis (left panel) and quantified in the right panel (each group $n = 3$, $^*P < 0.05$).

calpain activation and cell death in WFS1-knockdown NSC34 cells (Fig. 6*E*). To verify these observations in patient cells, we pretreated neural progenitor cells derived from iPSCs of a Wolfram syndrome patient and an unaffected parent with dantrolene, and then challenged these cells with thapisgargin. Thapsigargin-induced cell death was increased in neural progenitor cells derived from the Wolfram syndrome patient relative to those derived from the unaffected parent, and dantrolene could prevent cell death in the patient iPSC-derived neural progenitor cells (Fig. 6*F*). In addition, we treated brain-specific WFS1 knockout mice with dantrolene and observed evidence of suppressed calpain activation in brain lysates from these mice (Fig. 6*G*). Collectively, these results argue

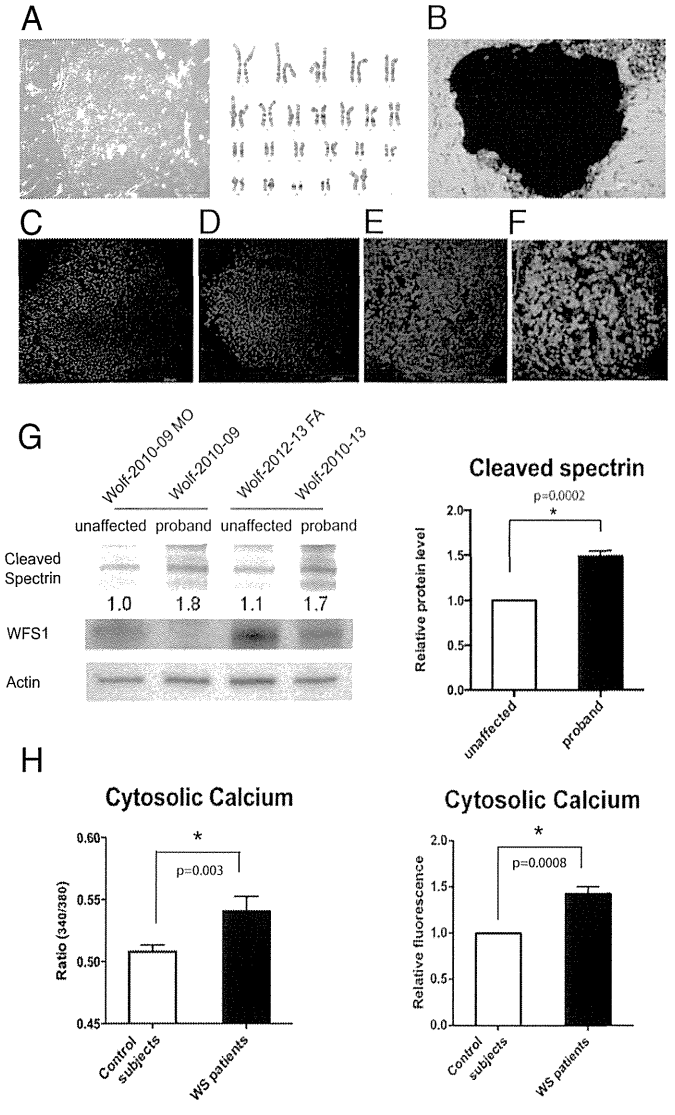

Fig. 5. High cytosolic calcium levels and hyperactivation of calpain in patient neural progenitor cells. (*A, Left*) Wolfram syndrome iPS cells derived from fibroblasts of a patient 1610. (*A, Right*) Karyotype of the Wolfram iPS cells. (*B*) Alkaline phosphatase staining of the Wolfram iPS cells. (*C–F*) Wolfram syndrome iPS cells stained with pluripotent markers: Nanog (*C*), Sox2 (*D*), SSEA4 (*E*), and TRA-1 (*F*). (*G*) Immunoblot analysis of cleaved spectrin and actin in neural progenitor cells derived from Wolfram syndrome patient iPS cells. The relative levels of the spectrin cleavage product are indicated (*Left*) and quantified (*Right*) ($n = 4$, $^*P < 0.05$). (*H, Left*) Quantitative analysis of cytosolic calcium levels in unaffected controls and Wolfram syndrome patients measured by Fura-2 calcium indicator (All values are means ± SEM; experiment was performed six independent times with >3 wells per sample each time; $n = 6$, $^*P < 0.05$). (*H, Right*) Quantification of cytosolic calcium levels in unaffected controls and Wolfram syndrome patients measured by Fluo-4 calcium assay (experiment was performed four independent times; $n = 4$, $^*P < 0.05$).

that dantrolene could prevent cell death in Wolfram syndrome by suppressing calpain activation.

Discussion

Growing evidence indicates that ER dysfunction triggers a range of human chronic diseases, including diabetes, atherosclerosis, inflammatory bowel disease, and neurodegenerative diseases (3, 4, 37–39). However, currently there is no effective therapy targeting the ER for such diseases due to the lack of clear understanding of the ER's contribution to the pathogenesis of these diseases. Although Wolfram syndrome is a rare disease and therefore not a focus of drug discovery efforts, the homogeneity of the patient population and disease mechanism has enabled us to identify a potential target, a calcium-dependent protease, calpain. Our results provide new insights into how the pathways leading to calpain activation cause β cell death and neurodegeneration, which are schematically summarized in Fig. 6*H*.

There are two causative genes for Wolfram syndrome, *WFS1* and *WFS2*. The functions of WFS1 have been extensively studied in pancreatic β cells. It has been shown that WFS1-deficient pancreatic β cells have high baseline ER stress levels and impaired insulin synthesis and secretion. Thus, WFS1-deficient β cells are susceptible to ER stress mediated cell death (5, 6, 32, 40–42). The functions of WFS2 are still not clear. There is evidence showing that impairment of WFS2 function can cause neural atrophy, muscular atrophy, and accelerate aging in mice (14). WFS2 has also been shown to be involved in autophagy (43). However, although patients with both genetic types of Wolfram syndrome suffer from the same disease manifestations, it was not clear if a common molecular pathway was altered in these patients. Our study has demonstrated, to our knowledge for the first time, that calpain hyperactivation is the common molecular pathway altered in patients with Wolfram syndrome. The mechanisms of calpain hyperactivation are different in the two genetic types of Wolfram syndrome. WFS1 mutations cause calpain activation by increasing cytosolic calcium levels, whereas WFS2 mutations lead to calpain activation due to impaired calpain inhibition.

Previously, Wolfram syndrome studies focused on pancreatic β cell function (5, 40, 41). However, patients also suffer from neuronal manifestations. MRI scans of Wolfram syndrome patients showed atrophy in brain tissue implying neurodegeneration in patients (7, 10). To investigate the mechanisms of neurodegeneration in Wolfram syndrome human cells, we established Wolfram syndrome iPSC-derived neural progenitor lines and confirmed the observations found in rodent cells and animal models of Wolfram syndrome. Differentiation of these iPSC-derived neural progenitor cells into specific types of neurons should be carried out in the future to better understand which cell types are damaged in Wolfram syndrome; this will lead to a better understanding of the molecular basis of this disease and provide cell models for future drug development.

Calpain activation has been found to be associated with type 2 diabetes and various neuronal diseases including Alzheimers, traumatic brain injury and cerebral ischemia, suggesting that regulation of calpains is crucial for cellular health (23). We discovered that calpain inhibitor III could confer protection against thapsigargin mediated cell death (Fig. 6*A*). Our data also demonstrates that calpeptin treatment was beneficial for cells with impaired WFS2 function. These results suggest that targeting calpain could be a novel therapeutic strategy for Wolfram syndrome. However, calpain is also an essential molecule for cell survival (44). Controlling calpain activation level is a double-bladed sword. We should carefully monitor calpain functions in treating patients with Wolfram syndrome (44).

Calpain activation is tightly regulated by cytosolic calcium levels. In other syndromes that increase cytosolic calcium level in pancreatic β cells, patients experience a transient or permanent period of hyperinsulinaemic hypoglycemia. This hyperinsulinaemic hypoglycemia can be partially restored by an inhibitor for ATP-sensitive potassium (K_{ATP}) channels or a calcium channel antagonist that prevents an increase in cytosolic calcium levels (45, 46). Although patients with Wolfram syndrome do not experience a period of hyperinsulinaemic hypoglycemia, small molecule compounds capable of altering cellular calcium levels may prevent calpain 2 activation and hold promise for treating patients with Wolfram syndrome. Treatment of WFS1-knockdown cells with dantrolene and ryanodine could prevent cell death mediated by WFS1 knockdown. Dantrolene is a muscle relaxant drug prescribed for multiple sclerosis, cerebral palsy or malignant hyperthermia (47). Dantrolene inhibits the ryanodine receptors and

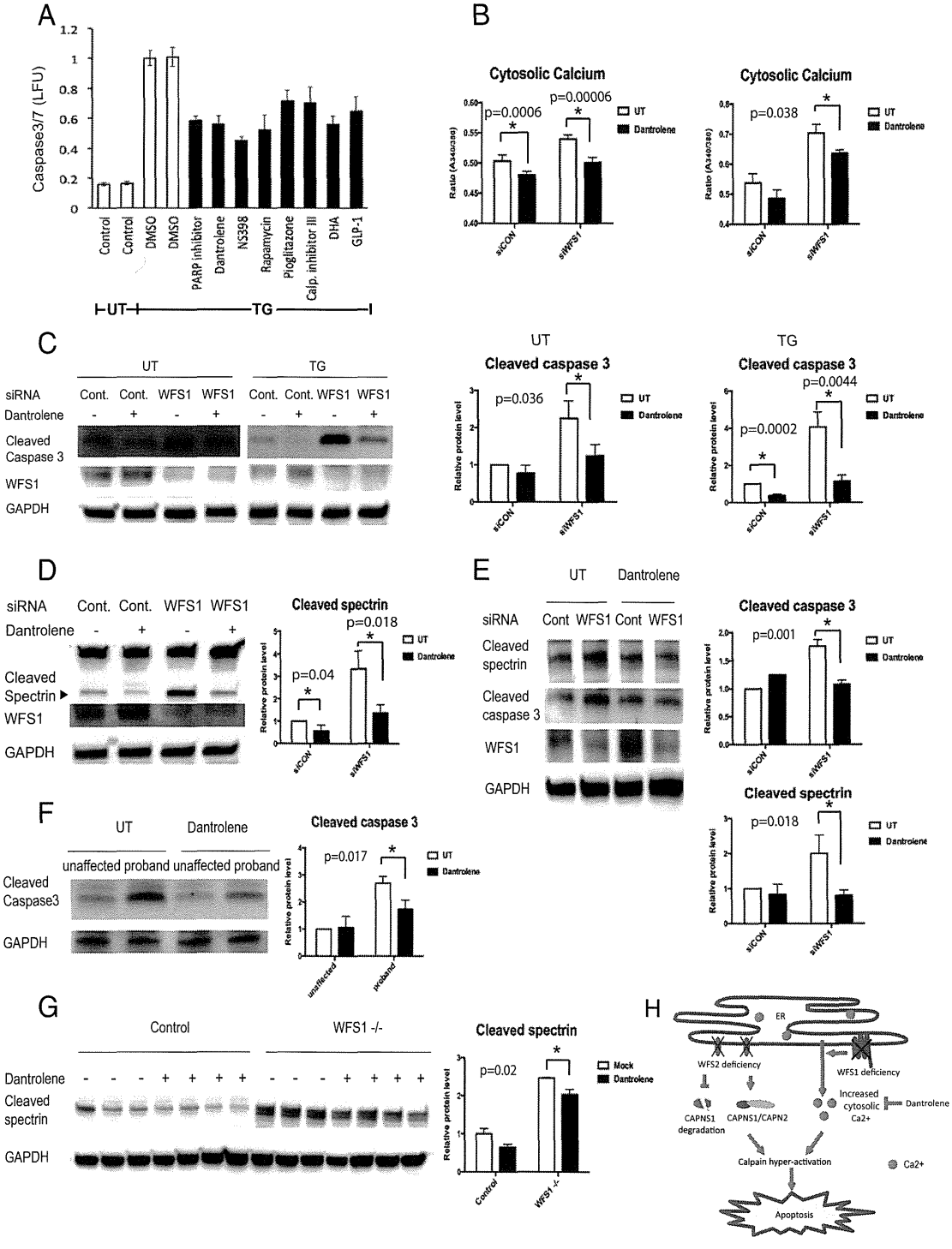

Fig. 6. Dantrolene prevents cell death in iPS cell-derived neural progenitor cells of Wolfram syndorme by inhibiting the ER calcium leakage to the cytosol. (*A*) INS-1 832/13 cells were pretreated with DMSO or drugs for 24 h then incubated in media containing 20 nM of thapsigargin (TG) overnight. Apoptosis was detected by caspase 3/7-Glo luminescence. (*B*) Cytosolic calcium levels were determined by Fura-2 in control and WFS1-deficient INS-1 832/13 (*Left*) and NSC34 (*Right*) cells treated or untreated with 10 μM dantrolene for 24 h (*All* values are means ± SEM; experiment was performed 6 independent times with >3 wells per sample each time $n = 6$, $^*P < 0.05$). (*C*) INS-1 832/13 cells were transfected with scrambled siRNA or siRNA against WFS1. Cells were pretreated with or without 10 μM dantrolene for 48 h, then incubated in media with or without 0.5 μM TG for 6 h. Expression levels of cleaved caspase-3, WFS1, GAPDH were measured by immunoblotting (*Left*). Protein levels of caspase3 under untreated (*Center*) and TG treated (*Right*) conditions are quantified and shown as bar graphs ($n = 3$, $^*P < 0.05$). (*D*) INS-1 832/13 cells were transfected with scrambled siRNA or siRNA against WFS1, pretreated with or without 10 μM dantrolene for 48 h, then incubated in media containing 0.5 μM TG for 6 h. Protein levels of cleaved spectrin, WFS1, GAPDH were analyzed by immunoblotting (*Left*) and quantified (*Right*) ($n = 3$, $^*P < 0.05$). (*E*) NSC34 cells were transfected with scrambled siRNA or siRNA against WFS1. Then treated with or without10 μM dantrolene for 24 h. Protein levels of cleaved spectrin, cleaved caspase 3, WFS2 and GAPDH were determined by immunoblotting (*Left*) and quantified (*Right*) ($n = 3$, $^*P < 0.05$). (*F*) Wolfram patient neural progenitor cells were pretreated with or without 10 μM dantrolene for 48 h. Then, cells were treated with 0.125 μM TG for 20 h. (*Left*) Apoptosis was monitored by immunoblotting. (*Right*) Quantification of cleaved caspase 3 protein levels are indicated ($n = 3$, $^*P < 0.05$). (*G*) Control and WFS1 brain-specific knockout mice were treated with water or dantrolene for 4 wk at 20 mg/kg. Brain lysates of these mice were examined by immunoblotting. Protein levels of cleaved spectrin and GAPDH were monitored (*Left*) and quantified (*Right*) (All values are means ± SEM; each group $n > 3$, $^*P < 0.05$). (*H*) Scheme of the pathogenesis of Wolfram syndrome.

reduces calcium leakage from the ER to cytosol, lowering cytosolic calcium level. The protective effect of dantrolene treatment on WFS1-deficient cells suggests that dysregulated cellular calcium homeostasis plays a role in the disease progression of Wolfram syndrome. In addition, it has been shown that stabilizing ER calcium channel function could prevent the progression of neurodegeneration in a mouse model of Alzheimer's disease (48). Therefore, modulating calcium levels may be an effective way to treat Wolfram syndrome or other ER diseases.

Dantrolene treatment did not block cell death mediated by WFS2 knockdown, suggesting that WFS2 does not directly affect the ER calcium homeostasis (Fig. S4 *D* and *E*). RNAi-mediated WFS1 knockdown in HEK293 cells significantly reduced the activation levels of sarco/endoplasmic reticulum calcium transport ATPase (SERCA), indicating that WFS1 may play a role in the modulation of SERCA activation and ER calcium levels (Fig. S5). It has been shown that WFS1 interacts with the Na^+/K^+ ATPase β1 subunit and the expression of WFS1 parallels that of Na^+/K^+ ATPase β1 subunit in a variety of settings, suggesting that WFS1 may function as an ion channel or regulator of existing channels (42). Further studies on this topic would be necessary to completely understand the etiology of Wolfram syndrome.

Our study reveals that dantrolene can prevent ER stress-mediated cell death in human and rodent cell models as well as mouse models of Wolfram syndrome. Thus, dantrolene and other drugs that regulate ER calcium homeostasis could be used to delay the progression of Wolfram syndrome and other diseases associated with ER dysfunction, including type 1 and type 2 diabetes.

Materials and Methods

Human Subjects. Wolfram syndrome patients were recruited through the Washington University Wolfram Syndrome International Registry website (wolframsyndrome.dom.wustl.edu). The clinic protocol was approved by the Washington University Human Research Protection Office and all subjects provided informed consent if adults and assent with consent by parents if minor children (IRB ID 201107067 and 201104010).

Animal Experiments. WFS1 brain-specific knockout mice were generated by breeding the Nestin-Cre transgenic mice (Jackson Laboratory) with WFS1 floxed mice (40). WFS2 whole body knockout mice are purchased from MRC Harwell. All animal experiments were performed according to procedures approved by the Institutional Animal Care and Use Committee at the Washington University School of Medicine (A-3381-01).

Calcium Levels. Calcium levels in cells were measured by Fura-2 AM dye and Fluo-4 AM dye (Life Technology) Inifinite M1000 (Tecan). Cells were plated in 96-well plates at 25,000 cells per well and stained with 4 μg/mL Fura-2 dye along with 2.5 mM probenecid for 30 min, then the cells were washed with PBS and kept in the dark for another 30 min to allow cleavage of AM ester. Fluorescence was measured at excitation wavelength 510 nm and emission wavelengths 340 nm and 380 nm. Then background subtractions were performed with both emission wavelengths. The subtraction result was used to calculate 340/380 ratios.

For Fluo-4 AM staining, neural progenitor cells were plated in 24-well plates at 200,000 cells per well. After staining with Fluo-4 AM dye for 30 min along with 2.5 mM probenecid, cells were washed and resuspended in PBS. Incubation for a further 30 min was performed to allow complete deesterification of intracellular AM esters. Then, samples were measured by flow cytometry at the FACS core facility of Washington University School of Medicine using a LSRII instrument (BD). The results were analyzed by FlowJo ver.7.6.3.

Statistical Analysis. Two-tailed *t* tests were used to compare the two treatments. *P* values below 0.05 were considered significant. All values are shown as means ± SD if not stated. Please see *SI Materials and Methods* for complete details.

ACKNOWLEDGMENTS. We thank all of the participants in the Washington University Wolfram Registry and Clinic and their families for their time and effort (wolframsyndrome.dom.wustl.edu/). We also thank Mai Kanekura, Mariko Hara, and Karen Sargent for technical support and the Washington University Wolfram Study Group Members and the study staff for advice and support in the greater research program. This work was supported by NIH Grants DK067493, P60 DK020579, and UL1 TR000448; Juvenile Diabetes Research Foundation Grants 47-2012-760 and 17-2013-512; American Diabetes Association Grant 1-12-CT-61, the Team Alejandro, The Team Ian, the Ellie White Foundation for Rare Genetic Disorders, and the Jack and J. T. Snow Scientific Research Foundation (F.U.).

1. Ron D, Walter P (2007) Signal integration in the endoplasmic reticulum unfolded protein response. *Nat Rev Mol Cell Biol* 8(7):519–529.
2. Tabas I, Ron D (2011) Integrating the mechanisms of apoptosis induced by endoplasmic reticulum stress. *Nat Cell Biol* 13(3):184–190.
3. Hetz C, Chevet E, Harding HP (2013) Targeting the unfolded protein response in disease. *Nat Rev Drug Discov* 12(9):703–719.
4. Wang S, Kaufman RJ (2012) The impact of the unfolded protein response on human disease. *J Cell Biol* 197(7):857–867.
5. Fonseca SG, et al. (2005) WFS1 is a novel component of the unfolded protein response and maintains homeostasis of the endoplasmic reticulum in pancreatic beta-cells. *J Biol Chem* 280(47):39609–39615.
6. Fonseca SG, et al. (2010) Wolfram syndrome 1 gene negatively regulates ER stress signaling in rodent and human cells. *J Clin Invest* 120(3):744–755.
7. Barrett TG, Bundey SE, Macleod AF (1995) Neurodegeneration and diabetes: UK nationwide study of Wolfram (DIDMOAD) syndrome. *Lancet* 346(8988):1458–1463.
8. Wolfram DJ, Wagener HP (1938) Diabetes mellitus and simple optic atrophy among siblings: Report of four cases. *Mayo Clin Proc* 1:715–718.
9. Urano F (2014) Diabetes: Targeting endoplasmic reticulum to combat juvenile diabetes. *Nat Rev Endocrinol* 10(3):129–130.
10. Hershey T, et al.; Washington University Wolfram Study Group (2012) Early brain vulnerability in Wolfram syndrome. *PLoS ONE* 7(7):e40604.
11. Marshall BA, et al.; Washington University Wolfram Study Group (2013) Phenotypic characteristics of early Wolfram syndrome. *Orphanet J Rare Dis* 8(1):64.
12. Inoue H, et al. (1998) A gene encoding a transmembrane protein is mutated in patients with diabetes mellitus and optic atrophy (Wolfram syndrome). *Nat Genet* 20(2):143–148.
13. Amr S, et al. (2007) A homozygous mutation in a novel zinc-finger protein, ERIS, is responsible for Wolfram syndrome 2. *Am J Hum Genet* 81(4):673–683.
14. Chen YF, et al. (2009) Cisd2 deficiency drives premature aging and causes mitochondria-mediated defects in mice. *Genes Dev* 23(10):1183–1194.
15. Wiley SE, et al. (2013) Wolfram Syndrome protein, Miner1, regulates sulphydryl redox status, the unfolded protein response, and Ca2+ homeostasis. *EMBO Mol Med* 5(6):904–918.
16. Shang L, et al. (2014) β-cell dysfunction due to increased ER stress in a stem cell model of Wolfram syndrome. *Diabetes* 63(3):923–933.
17. Sandhu MS, et al. (2007) Common variants in WFS1 confer risk of type 2 diabetes. *Nat Genet* 39(8):951–953.
18. Bonnycastle LL, et al. (2013) Autosomal dominant diabetes arising from a Wolfram syndrome 1 mutation. *Diabetes* 62(11):3943–3950.
19. Goll DE, Thompson VF, Li H, Wei W, Cong J (2003) The calpain system. *Physiol Rev* 83(3):731–801.
20. Tan Y, et al. (2006) Ubiquitous calpains promote caspase-12 and JNK activation during endoplasmic reticulum stress-induced apoptosis. *J Biol Chem* 281(23):16016–16024.
21. Tan Y, Wu C, De Veyra T, Greer PA (2006) Ubiquitous calpains promote both apoptosis and survival signals in response to different cell death stimuli. *J Biol Chem* 281(26):17689–17698.
22. Nakagawa T, Yuan J (2000) Cross-talk between two cysteine protease families. Activation of caspase-12 by calpain in apoptosis. *J Cell Biol* 150(4):887–894.
23. Cui W, et al. (2013) Free fatty acid induces endoplasmic reticulum stress and apoptosis of β-cells by Ca2+/calpain-2 pathways. *PLoS ONE* 8(3):e59921.
24. Huang CJ, et al. (2010) Calcium-activated calpain-2 is a mediator of beta cell dysfunction and apoptosis in type 2 diabetes. *J Biol Chem* 285(1):339–348.
25. Barrett TG, Bundey SE (1997) Wolfram (DIDMOAD) syndrome. *J Med Genet* 34(10):838–841.
26. Liu MC, et al. (2006) Comparing calpain- and caspase-3-mediated degradation patterns in traumatic brain injury by differential proteome analysis. *Biochem J* 394(Pt 3):715–725.
27. Hara T, et al. (2014) Calcium efflux from the endoplasmic reticulum leads to β-cell death. *Endocrinology* 155(3):758–768.
28. Takei D, et al. (2006) WFS1 protein modulates the free Ca(2+) concentration in the endoplasmic reticulum. *FEBS Lett* 580(24):5635–5640.
29. Liu MC, et al. (2006) Extensive degradation of myelin basic protein isoforms by calpain following traumatic brain injury. *J Neurochem* 98(3):700–712.
30. Takahashi K, Yamanaka S (2006) Induction of pluripotent stem cells from mouse embryonic and adult fibroblast cultures by defined factors. *Cell* 126(4):663–676.
31. Yusta B, et al. (2006) GLP-1 receptor activation improves beta cell function and survival following induction of endoplasmic reticulum stress. *Cell Metab* 4(5):391–406.
32. Akiyama M, et al. (2009) Increased insulin demand promotes while pioglitazone prevents pancreatic beta cell apoptosis in Wfs1 knockout mice. *Diabetologia* 52(4):653–663.
33. Bachar-Wikstrom E, et al. (2013) Stimulation of autophagy improves endoplasmic reticulum stress-induced diabetes. *Diabetes* 62(4):1227–1237.
34. Dykes MH (1975) Evaluation of a muscle relaxant: Dantrolene sodium (Dantrium). *JAMA* 231(8):862–864.

35. Wei H, Perry DC (1996) Dantrolene is cytoprotective in two models of neuronal cell death. *J Neurochem* 67(6):2390–2398.
36. Luciani DS, et al. (2009) Roles of IP3R and RyR Ca2+ channels in endoplasmic reticulum stress and beta-cell death. *Diabetes* 58(2):422–432.
37. Hotamisligil GS (2010) Endoplasmic reticulum stress and atherosclerosis. *Nat Med* 16(4):396–399.
38. Hotamisligil GS (2010) Endoplasmic reticulum stress and the inflammatory basis of metabolic disease. *Cell* 140(6):900–917.
39. Ozcan L, Tabas I (2012) Role of endoplasmic reticulum stress in metabolic disease and other disorders. *Annu Rev Med* 63:317–328.
40. Riggs AC, et al. (2005) Mice conditionally lacking the Wolfram gene in pancreatic islet beta cells exhibit diabetes as a result of enhanced endoplasmic reticulum stress and apoptosis. *Diabetologia* 48(11):2313–2321.
41. Ishihara H, et al. (2004) Disruption of the WFS1 gene in mice causes progressive beta-cell loss and impaired stimulus-secretion coupling in insulin secretion. *Hum Mol Genet* 13(11):1159–1170.
42. Zatyka M, et al. (2008) Sodium-potassium ATPase 1 subunit is a molecular partner of Wolframin, an endoplasmic reticulum protein involved in ER stress. *Hum Mol Genet* 17(2):190–200.
43. Chang NC, Nguyen M, Germain M, Shore GC (2010) Antagonism of Beclin 1-dependent autophagy by BCL-2 at the endoplasmic reticulum requires NAF-1. *EMBO J* 29(3): 606–618.
44. Dutt P, et al. (2006) m-Calpain is required for preimplantation embryonic development in mice. *BMC Dev Biol* 6:3.
45. Arya VB, Mohammed Z, Blankenstein O, De Lonlay P, Hussain K (2014) Hyperinsulinaemic hypoglycaemia. *Hormone Metabolic Res* 46(3):157–170.
46. Shah P, Demirbilek H, Hussain K (2014) Persistent hyperinsulinaemic hypoglycaemia in infancy. *Semin Pediatr Surg* 23(2):76–82.
47. Krause T, Gerbershagen MU, Fiege M, Weisshorn R, Wappler F (2004) Dantrolene—a review of its pharmacology, therapeutic use and new developments. *Anaesthesia* 59(4):364–373.
48. Chakroborty S, et al. (2012) Stabilizing ER Ca2+ channel function as an early preventative strategy for Alzheimer's disease. *PLoS ONE* 7(12):e52056.

nature COMMUNICATIONS

ARTICLE

Received 24 Jan 2014 | Accepted 2 Oct 2014 | Published 14 Nov 2014

DOI: 10.1038/ncomms6464 OPEN

The role of maternal-specific H3K9me3 modification in establishing imprinted X-chromosome inactivation and embryogenesis in mice

Atsushi Fukuda[1], Junko Tomikawa[2], Takumi Miura[1], Kenichiro Hata[2], Kazuhiko Nakabayashi[2], Kevin Eggan[3], Hidenori Akutsu[1] & Akihiro Umezawa[1]

Maintaining a single active X-chromosome by repressing *Xist* is crucial for embryonic development in mice. Although the *Xist* activator RNF12/RLIM is present as a maternal factor, maternal *Xist* (Xm-*Xist*) is repressed during preimplantation phases to establish imprinted X-chromosome inactivation (XCI). Here we show, using a highly reproducible chromatin immunoprecipitation method that facilitates chromatin analysis of preimplantation embryos, that H3K9me3 is enriched at the *Xist* promoter region, preventing Xm-*Xist* activation by RNF12. The high levels of H3K9me3 at the *Xist* promoter region are lost in embryonic stem (ES) cells, and ES-cloned embryos show RNF12-dependent *Xist* expression. Moreover, lack of Xm-XCI in the trophectoderm, rather than loss of paternally expressed imprinted genes, is the primary cause of embryonic lethality in 70–80% of parthenogenotes immediately after implantation. This study reveals that H3K9me3 is involved in the imprinting that silences Xm-*Xist*. Our findings highlight the role of maternal-specific H3K9me3 modification in embryo development.

[1] Department of Reproductive Biology, National Research Institute for Child Health and Development, 2-10-1 Okura, Setagaya, Tokyo 157-8535, Japan. [2] Department of Maternal-Foetal Biology, National Research Institute for Child Health and Development, 2-10-1 Okura, Setagaya, Tokyo 157-8535, Japan. [3] The Howard Hughes Medical Institute, Harvard Stem Cell Institute and the Department of Stem Cell and Regenerative Biology, Harvard University, 7 Divinity Avenue, Cambridge, Massachusetts 02138, USA. Correspondence and requests for materials should be addressed to H.A. (email: akutsu-h@ncchd.go.jp).

To maintain proper dosage compensation in mammals, one of the two X chromosomes in the female is inactivated[1,2]. In establishment of X-chromosome inactivation (XCI), a large non-coding RNA, *Xist*, is expressed and this non-coding RNA then covers the entire X chromosome in *cis*[1–3]. In mice, two types of XCI occur during female embryonic development. One type involves random XCI, which is observed in cells derived from epiblasts, and one of the two X chromosomes (paternal or maternal) is randomly inactivated. The other involves imprinted XCI (iXCI), which is observed in extra-embryonic tissues and causes XCI of the paternal X chromosome (Xp)[4]. The initiation of iXCI begins at early preimplantation in embryos and Xp-*Xist* is expressed around the four-cell stage[1]. A recent study showed that a maternal factor, the E3 ubiquitin ligase RNF12, is the primary factor responsible for Xp-*Xist* activation[5]. Interestingly, although RNF12 is abundant as a maternal factor in oocytes, Xm-*Xist* is not expressed. Moreover, maternal *Xist* (Xm-*Xist*)-specific imprints, which are refractory to the Xm-*Xist* activation induced by RNF12, are imposed during oogenesis[6]. *Xist* expression analysis using *de novo* DNA methyltransferase (*Dnmt3a/b*) maternal knockout mice demonstrated that *Xist* expression during preimplantation is independent of DNA methylation[7], implying that other epigenetic factors are associated with Xm-*Xist* silencing. However, the nature of these Xm-specific epigenetic modifications is unknown.

A gene-knockout study demonstrated that loss of Xp-*Xist* expression critically affects postimplantation female development due to lack of iXCI, which causes overexpression of X-linked genes in extra-embryonic tissues[8]. Similar to the phenotype observed in Xp-*Xist*-knockout mice, parthenogenetic embryos (PEs) composed of two X chromosomes show increased expression of X-linked genes, as compared with fertilized females, because of the low expression of *Xist*[9]. One of the interesting phenomena observed in PEs is the dramatic developmental failure that occurs immediately after implantation. Around 70–80% of embryos die before embryonic day (E) 9.5, which is the limit of development for PEs[10]. However, it is unknown whether the primary cause of rapid developmental failure in postimplantation PEs is the loss of iXCI or the loss of expression of autosomal paternally imprinted genes[11,12].

The global epigenetic asymmetry of parental genomes in zygotes is retained during early preimplantation phases in mice and changes in gene expression occur in discrete stages to confer totipotency[13,14]. Interestingly, transcriptionally repressive marks, such as histone H3 lysine 9 di-/trimethylation (H3K9me2/3), are specifically imposed on maternal genomes at the zygote stage[13]. Although the regulation of imprinted genes mostly depends on DNA methylation, some imprinted genes are regulated by these histone modifications[15,16]. Thus, Xm-*Xist* silencing machinery may be associated with histone modifications.

Here we reveal that silencing of Xm-*Xist* in preimplantation embryos involves modification of H3K9me3. By using a new chromatin immunoprecipitation (ChIP) method that facilitates chromatin analysis in preimplantation embryos, we show that the *Xist* promoter on the Xm is highly enriched for H3K9me3 at the four-cell stage. This enrichment is lost in the morula and in male embryonic stem (ES) cells. Furthermore, we demonstrate that early loss of H3K9me3 at the *Xist* promoter leads to precocious Xm-*Xist* activation in a Rnf12-dependent manner. Moreover, we demonstrate that establishment of Xm-XCI in the trophectoderm allows PEs to develop at the postimplantation stage without the expression of paternally imprinted genes on autosomes. Therefore, these data indicate that the primary cause of embryonic lethality immediately after implantation in most PEs is loss of XCI rather than loss of the expression of paternally imprinted genes located on autosomes. Our study revealed that silencing of Xm-*Xist* by imprinting to establish iXCI involves H3K9me3, and this finding is expected to resolve the longstanding issues that have limited our general understanding of XCI in mice.

Results

Changes in histone modifications cause Xm-*Xist* derepression. Histone repressive marks, such as H3K9me2/3 and H3K27me3, are specifically imposed on maternal genomes[13]. To investigate the role of maternal-specific modifications in imprinted *Xist* expression, we focused on *Kdm3a* and *Kdm4b*, which encode histone demethylases specific for H3K9me1/2 and H3K9me3 (refs 17,18), respectively. Reverse transcription–PCR analysis showed that oocytes express low levels of *Kdm3a* and *Kdm4b* (Supplementary Fig. 1). Immunofluorescence (IF) analyses revealed that zygotes injected with polyadenylated *Kdm3a* and *Kdm4b* messenger RNAs expressed significantly lower levels of maternal H3K9me2 and H3K9me3, respectively (Fig. 1a–d). Ectopic expression of *Kdm3a* and *Kdm4b* did not affect H3K9me3 or H3K9me2 marks, respectively (Supplementary Fig. 2). We reasoned that if Xm-specific modifications that prevent *Xist* activation were erased by these epigenetic modifiers, Xm-*Xist* would be expressed at the four-cell stage, which is when Xp-*Xist* expression commences.

To facilitate analysis of Xm-*Xist* expression, we used PEs (Fig. 1e). PEs possess two copies of Xm, and Xm-*Xist* is never expressed at the four-cell stage[19]. Xm-*Xist* expression in four-cell PEs, cultured for 48 h, was determined using quantitative real-time PCR (qPCR). Consistent with a previous report[19], Xm-*Xist* was not detectably expressed in most intact (not injected) PEs and PEs injected with *Egfp* mRNA (*Egfp*-PEs; Fig. 1f). Approximately 75% of PEs injected with *Kdm3a* mRNA (*Kdm3a*-PEs) did not detectably express *Xist*. However, Xm-*Xist* expression was detected in all PEs injected with *Kdm4b* mRNA (*Kdm4b*-PEs;

Figure 1 | Alterations in histone modifications derepress Xm-*Xist* expression. (**a**–**d**) Oocytes injected with *Kdm3a* (**a**,**b**), *Kdm4b* (**c**,**d**) or *Egfp* mRNAs were subjected to ICSI. After 7–8 h, embryos were fixed and analysed for H3K9me2 (**a**) and H3K9me3 (**c**) using IF. Nuclei stained with 4′,6-diamidino-2-phenylindole (DAPI) are shown in blue. Representative images are presented on the left. The box-and-whisker plot shows the ratio of maternal to paternal signal intensities. The horizontal line indicates the median. The *P*-values were calculated using the Mann–Whitney *U*-test (*U*-test). Pb, polar body; *n*, number of embryos analysed (**b**,**d**). (**e**) Schema of the generation of PEs with altered histone modifications. To examine the effects of histone demethylation on Xm-*Xist* expression, either H3K9me2 demethylase (*Kdm3a*) or H3K9me3 demethylase (*Kdm4b*) mRNAs were injected into MII oocytes that were then activated. To assess the effects of inhibition of histone deacetylation on Xm-*Xist* expression, oocytes were activated and incubated in the presence of TSA for 24 h. After 48 h, ten four-cell PEs were pooled and analysed as one biological replicate using qPCR. (**f**) Analysis of Xm-*Xist* expression at the four-cell stage. The expression level of Xm-*Xist* in female embryos derived from IVF was defined as 1. One or two asterisks indicate Xm-*Xist* expression in one or two replicates, respectively. The *P*-values were determined using Student's *t*-tests. Error bars indicate the mean ± s.e.m. (**g**–**i**) *Xist* FISH analysis of *Kdm4b*- and *Egfp* + TSA-PEs at the four-cell stage. (**g**) Representative images of FISH results. (**h**) Ratio of cells with *Xist* signal to the total number of cells. *n*, number of interphase cells analysed. (**i**) Ratio of cells with biallelic expression to total cells. The detailed FISH results are shown in Supplementary Table 1. Scale bars, 20 μm.

Fig. 1f), suggesting that H3K9me3 demethylation caused Xm-*Xist* derepression.

We next assessed the effects of a histone deacetylase inhibitor, trichostatin A (TSA), on Xm-*Xist* expression. TSA-treated PEs (Intact + TSA-PEs and *Egfp* + TSA-PEs) also activated Xm-*Xist* (Fig. 1f). No significant changes were detected in Xm-*Xist* expression levels between *Kdm4b*-PEs and *Egfp* + TSA-PEs. However, although co-injection with *Kdm4b* and *Kdm3a* mRNAs did not increase Xm-*Xist* expression levels as compared with *Kdm4b*-PEs, a combination of TSA and *Kdm4b*-mRNA significantly increased Xm-*Xist* expression as compared with *Egfp* + TSA-PEs (2.9-fold, $P<0.04$, Student's *t*-test; Fig. 1f). Moreover, derepression of Xm-*Xist* transcription occurred in the absence of *Rnf12* overexpression (Supplementary Fig. 3), and *Jpx* and *Ftx*,

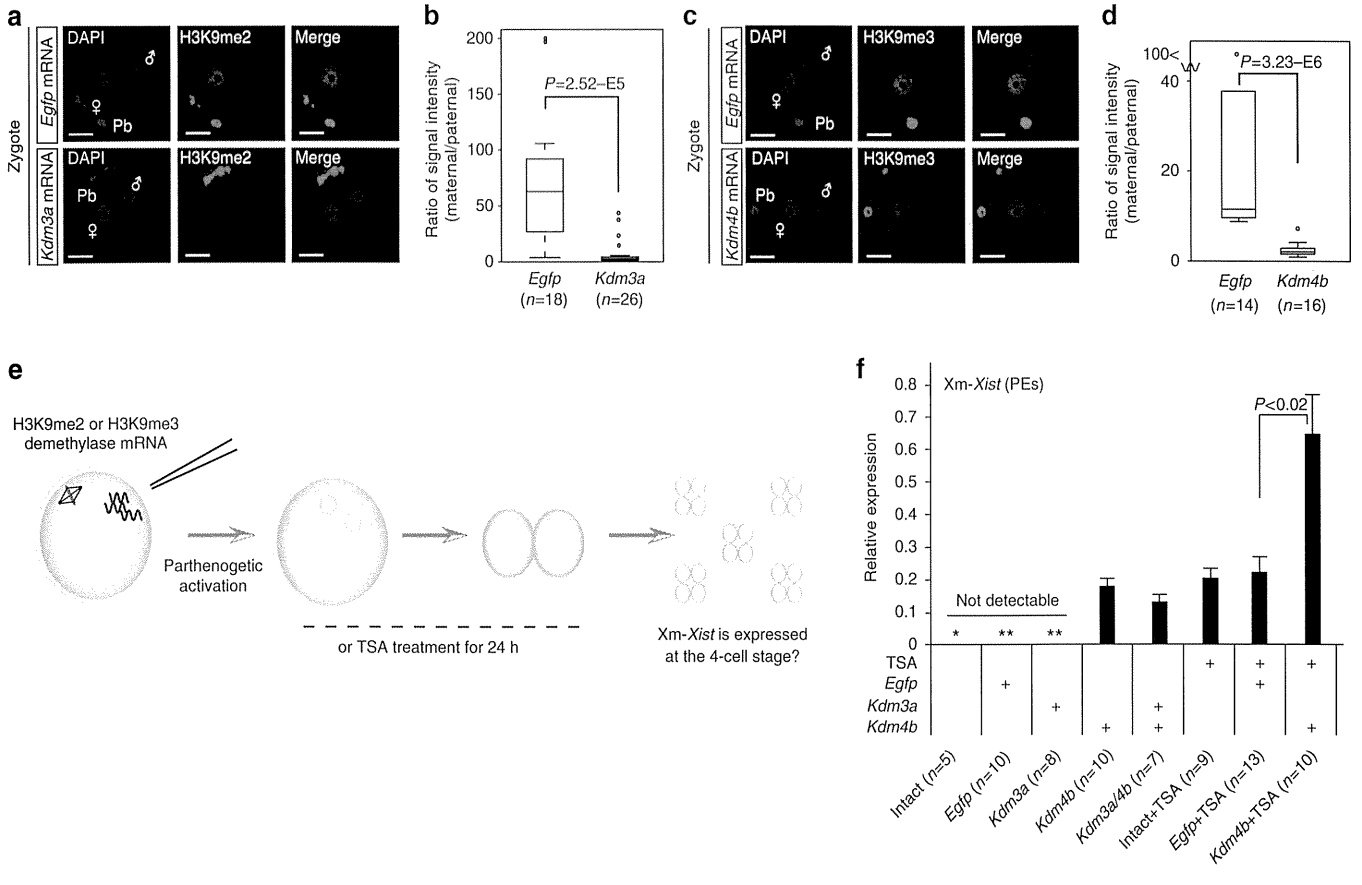

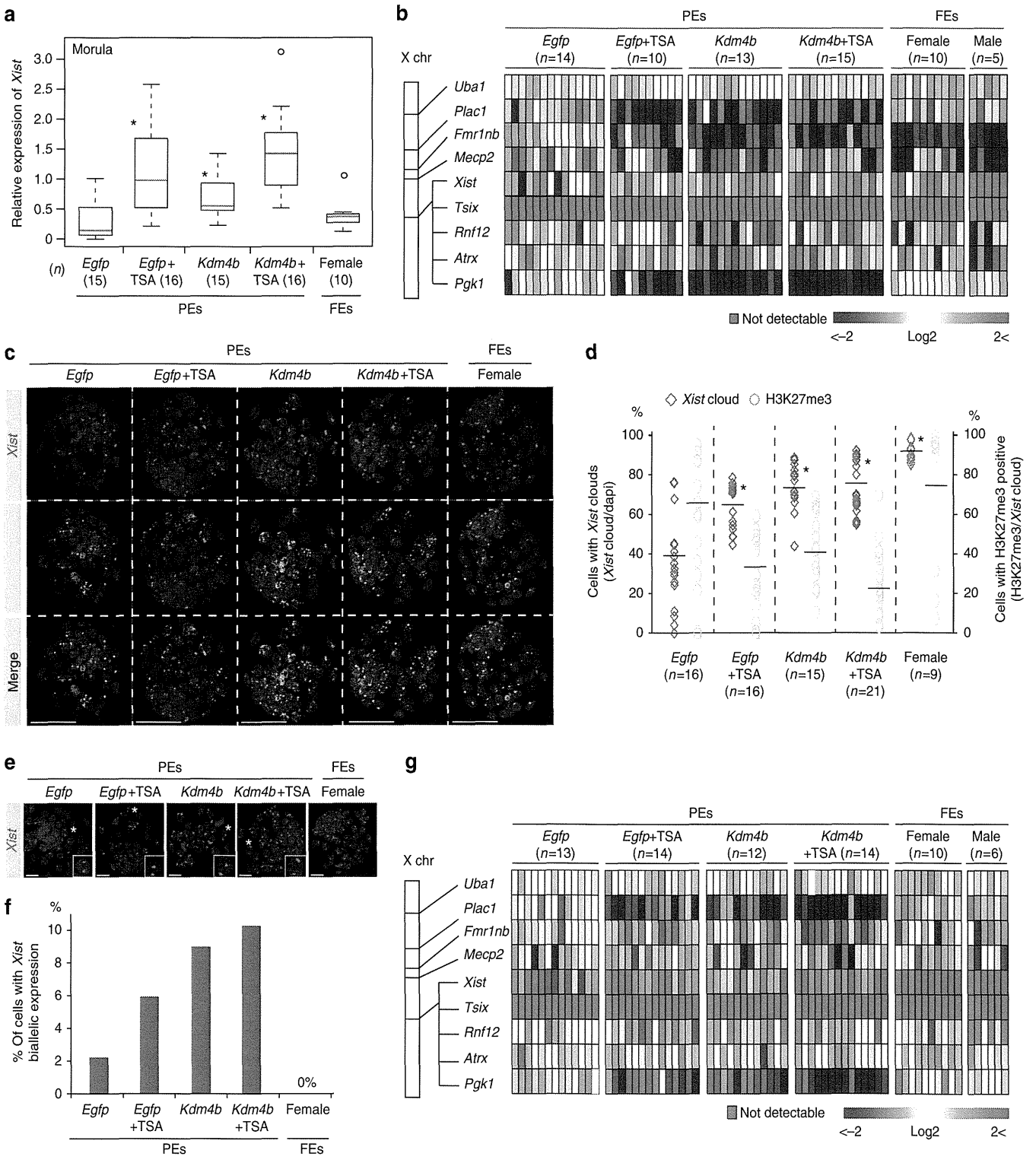

Figure 2 | Global XCI and *Xist* expression states of Xm at late preimplantation stages. (**a**) Analysis of *Xist* expression using qPCR of individual embryos in the morula. An asterisk indicates $P<0.05$ (Student's *t*-test) compared with *Egfp*-PEs. FEs, fertilized embryos. (**b**) Large-scale qPCR analysis of *Xist* and eight X-linked genes in individual blastocysts after culturing for 96 h. Coloured bars indicate expression levels. (**c**,**d**) IF (H3K27me3, green) combined with RNA FISH (*Xist*, red) analysis in 96-h blastocyst stage. 4′,6-diamidino-2-phenylindole (DAPI)-stained nuclei are shown in blue. (**c**) Representative confocal projection. Scale bars, 50 μm. (**d**) The graph shows *Xist* expression and H3K27me3 modification states in individual embryos. The horizontal axis indicates the average percentage in the group. $^{*}P<3.1\times10^{-28}$ (Fisher's exact test). *n*, number of embryos analysed. (**e**,**f**) Xm-*Xist* biallelic expression states in PEs at 96 h. The asterisk indicates cells with biallelic expression. Scale bars, 20 μm. (**f**) Summary of the ratio of biallelic cells to *Xist*-positive cells in 96-h blastocyst stage in each group. The number of cells is shown in Supplementary Table 3. (**g**) qPCR analysis of *Xist* and eight X-linked genes in individual blastocysts after culturing for 120 h. (**h**,**i**) IF (H3K27me3, green) combined with RNA FISH (*Xist*, red) analysis in 120 h blastocysts. $^{*}P<5.4\times10^{-23}$ (Fisher's exact test). Scale bars, 50 μm. (**j**) The ratio of biallelic cells to *Xist*-positive cells in 120 h blastocysts. In qPCR analysis, the average expression level of Xm-*Xist* in *Egfp*-PEs was set as 1 (also see the Methods section). *Gapdh* and *β-actin* were used as internal controls. Data are summarized in Supplementary Table 4.

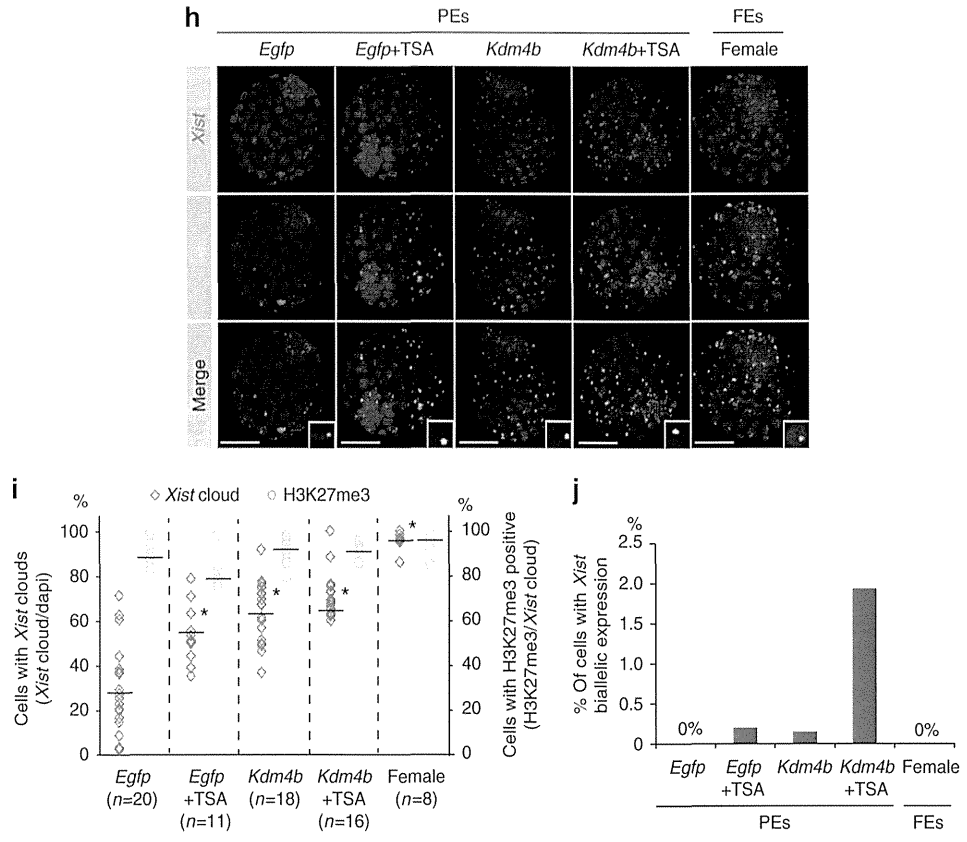

Figure 2 | Continued.

which have been identified as *Xist* activators[2], were not expressed at the four-cell stage. These results showed that KDM4B- and TSA-mediated Xm-*Xist* derepression was not involved in the abnormal expression of known *Xist* activators.

Next, we examined Xm-*Xist* derepression states at the single-cell level by fluorescence *in situ* hybridisation (FISH) of *Xist* RNA. Consistent with the qPCR results, Xm-*Xist* signals were significantly increased in *Egfp* + TSA- and *Kdm4b*-PEs (Fig. 1g,h and Supplementary Table 1). However, neither TSA treatment nor *Kdm4b* overexpression consistently activated Xm-*Xist* in all cells (Fig. 1g,h). FISH analysis also revealed *Xist* biallelic cells in *Kdm4b*- and *Egfp* + TSA-PEs (*Kdm4b*-PEs: 34% and *Egfp* + TSA-PEs: 13%; Fig. 1g,i). Taken together, these results indicated that *Kdm4b* overexpression and TSA treatment induced Xm-*Xist* derepression at the same developmental stage as Xp-*Xist* activation.

Xm-*Xist* transcripts establish XCI at the blastocyst stage. To investigate whether Xm-*Xist* transcripts from the four-cell stage induced XCI in late preimplantation stages, we cultured *Kdm4b*-, *Egfp* + TSA- and *Kdm4b* + TSA-PEs until the blastocyst stage. Development into blastocysts occurred in >80% of PEs in all groups (Supplementary Table 2). At the morula stage (72 h), although *Egfp*-PEs initiated Xm-*Xist* expression, the levels of *Xist* expression were significantly lower compared with those in *Kdm4b*-injected and/or TSA-treated PEs (Fig. 2a). At the 96-h blastocyst stage, we examined the expression levels of *Xist* and X-linked genes (*Tsix*, *Rnf12*, *Pgk1*, *Fmr1nb*, *Atrx*, *Uba1*, *Mecp2* and *Plac1*) in individual embryos. The significant upregulation of *Xist* observed in PEs that had been injected with *Kdm4b* mRNA and/or TSA continued in 96-h blastocyst stage (Fig. 2b). In PEs exhibiting Xm-*Xist* upregulation, *Tsix* expression was not detectable and *Rnf12* was not overexpressed as compared with *Egfp*-PEs (Fig. 2b). The average expression levels of *Pgk1*, *Plac1* and *Fmr1nb* in *Kdm4b*-overexpressing or TSA-treated PE groups were significantly reduced (Supplementary Fig. 4a). However, single embryos in the same group exhibited heterogeneity in the expression levels of these targets (Fig. 2b). Moreover, although Xm-*Xist* was not overexpressed in *Kdm4b*-overexpressing or TSA-treated PE groups compared with levels seen in female fertilized embryos (FEs), the levels of *Plac1* and *Pgk1* were strongly downregulated in *Kdm4b*-, *Egfp* + TSA- and *Kdm4b* + TSA groups (Fig. 2b). These results suggested that Xm-*Xist* expression states differed at the single-cell level in individual embryos.

To gain further insights into *Xist* expression states and repression of X-linked genes on Xm alleles, we conducted IF to detect the H3K27me3 state, which is a hallmark of XCI[20], and performed *Xist* FISH analysis. The *Xist* RNA FISH probe recognizes *Xist* and *Tsix*. Therefore, the cloud state of the FISH signal defined *Xist* expression. Consistent with the qPCR results, the number of cells with *Xist* signals increased significantly in all *Kdm4b*-overexpressing or TSA-treated PEs (Fig. 2c and Supplementary Table 3). However, in all *Kdm4b*-overexpressing or TSA-treated PEs, <45% of *Xist* cloud-containing cells had an H3K27me3 signal (Fig. 2c,d and Supplementary Table 3). We also found that *Xist* biallelic cells were present in all PE groups (*Egfp*-PEs: 2.2%, *Egfp* + TSA-PEs: 5.9%, *Kdm4b*-PEs: 9.0% and *Kdm4b* + TSA-PEs: 10.3%; Fig. 2e,f). These results suggested that there were various Xm-*Xist* expression states present at the single-cell level, affecting the heterogeneity of X-linked genes, and that strong suppression of some X-linked genes in *Kdm4b*-overexpressing or TSA-treated PEs could be attributed to biallelic expression of Xm-*Xist*.

As *Kdm4b* overexpression and TSA treatment did not affect the extent of H3K27me3 modification (Supplementary Fig. 5), its acquisition in PEs may have been slightly delayed compared with that in FEs. In support of this notion, the developmental timing of PEs lags behind that of FEs[9]. Therefore, we extended the culture period to 120 h and again performed qPCR, IF and FISH analyses.

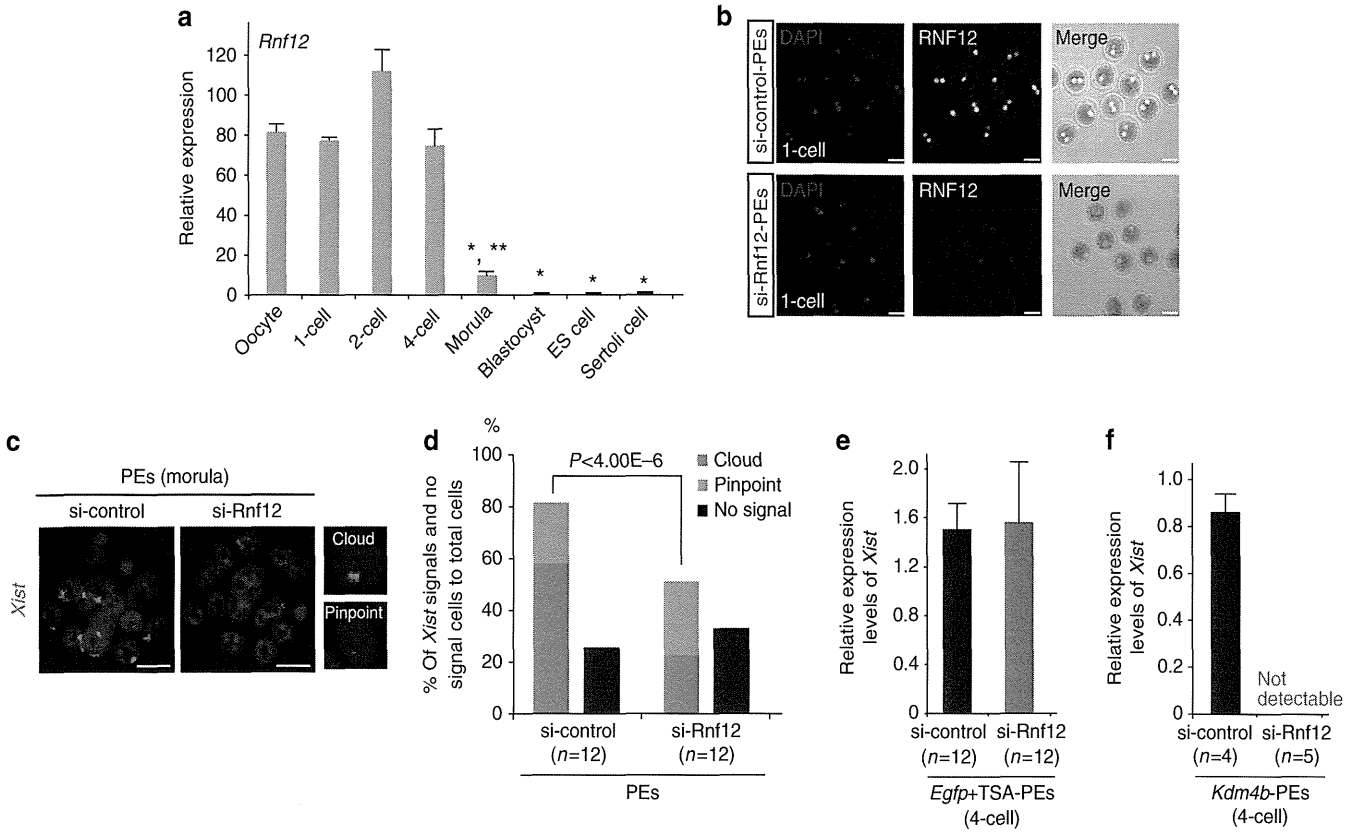

Figure 3 | RNF12 is required for *Xist* expression in various types of preimplantation embryos. (**a**) *Rnf12* expression profiles in preimplantation stages, ES cells and somatic cells. Ten oocytes ($n=3$), ten IVF-1 cells ($n=3$), ten IVF-2 cells ($n=3$) and five IVF-4 cells ($n=3$) were pooled. The expression level of *Rnf12* in the morula stage, as determined using qPCR, represents the average of 16 individual embryos. The numbers of ES and Sertoli cells represent the averages of three independent cell lines and male pups, respectively. The error bars indicate the mean ± s.e.m. *$P<0.004$ compared with oocytes; **$P<0.0001$ compared with ES cells (Student's *t*-test). (**b**) IF analysis of RNF12 at the one-cell stage (green). Samples were fixed 11 h after parthenogenetic activation (18–19 h after siRNA injection). The same laser beam intensities were used to excite the *Rnf12*-knockdown and control samples. 4′,6-diamidino-2-phenylindole (DAPI)-stained nuclei are shown in blue. Two independent experiments were conducted. Scale bars, 50 μm. (**c**,**d**) *Xist* FISH analysis of si-Rnf12 PEs at the morula stage. At 72 h after activation, PEs injected with siRNA were analysed. Representative images of siRNA-treated embryos (**c**). Scale bars, 20 μm. The percentage of total *Xist*-positive signals and -negative cells to total cells in si-Rnf12 and si-control PEs. Biallelic expression was counted as two signals. *n*, number of embryos analysed (**d**). (**e**,**f**) qPCR analysis of Xm-*Xist* expression at the four-cell stage of embryos treated with TSA (**e**) or injected with *Kdm4b* mRNA (**f**). PEs derived from maternal si-Rnf12-treated oocytes. A detailed experimental scheme is shown in Supplementary Fig. 6d. A pool of eight to ten four-cell embryos represents one biological replicate.

As seen in 96-h blastocyst stage, qPCR analysis revealed that *Plac1* and *Pgk1* were significantly repressed in *Kdm4b*-overexpressing or TSA-treated PEs, although heterogeneity was observed (Fig. 2g and Supplementary Fig. 4b). However, *Fmr1nb*, which was significantly repressed in 96-h blastocyst stage of both *Kdm4b*- and TSA-treated groups, did not show marked suppression (Fig. 2g and Supplementary Fig. 4b), suggesting that *Xist* expression states were altered in 120 h blastocysts.

In FISH and IF analysis, a significant increase in the number of *Xist*-positive cells was detected in *Kdm4b*-overexpressing and/or TSA-treated PEs, as compared with *Egfp*-PEs, after culture for 120 h (Fig. 2h,i and Supplementary Table 4). There was a marked increase in the ratio of H3K27me3 spots to cloud *Xist* signals in blastocysts in all groups compared with that observed after 96 h of culture as follows: 88.1% in *Egfp*-PEs, 78.7% in *Egfp* + TSA-PEs, 91.8% in *Kdm4b*-PEs and 91.2% in *Kdm4b* + TSA-PEs (Fig. 2h,i and Supplementary Table 4). Interestingly, >98% of the cells in the *Xist* cloud state exhibited monoallelic *Xist* expression in all groups at 120 h (Fig. 2j).

Taken together, these results indicated that *Kdm4b* overexpression and TSA treatment induced global XCI of Xm in blastocysts and that the counting mechanism automatically functioned in late blastocysts, as has also been observed for Xp alleles[21].

KDM4B-mediated Xm-*Xist* expression depends on RNF12. During preimplantation phases, Xp-*Xist* expression is induced by maternal RNF12 (ref. 5). Thus, we investigated whether Xm-*Xist* expression also depended on RNF12. High *Rnf12* expression levels were maintained until the four-cell stage (around 80-fold higher than in ES cells; Fig. 3a). At the morula stage, although the expression level was significantly decreased compared with that in oocytes, *Rnf12* expression was still more than ninefold higher than that in ES cells (Fig. 3a), indicating that maternal and early zygotic RNF12 may be critical for Xm-*Xist* activation. To examine the dependency of RNF12 on Xm-*Xist* expression, we inhibited maternal and zygotic RNF12 expression using *Rnf12*-siRNA (Supplementary Fig. 6a). IF analysis at the one-cell stage showed a marked decline in RNF12 signal intensity in si-*Rnf12* embryos compared with that in the si-control embryos (Fig. 3b). Significant repression by si-*Rnf12* was maintained in the four-cell stage (Supplementary Fig. 6b,c). Using this knockdown system, we examined whether Xm-*Xist* activation was induced by RNF12 at the morula stage. *Xist* FISH analysis revealed that *Xist* signals (cloud and pinpoint) in PEs treated with si-Rnf12 were significantly reduced at the morula stage as compared with those observed in the controls (si-Rnf12: 50.0% versus si-control: 80.0%; Fig. 3c,d and Supplementary Table 5).

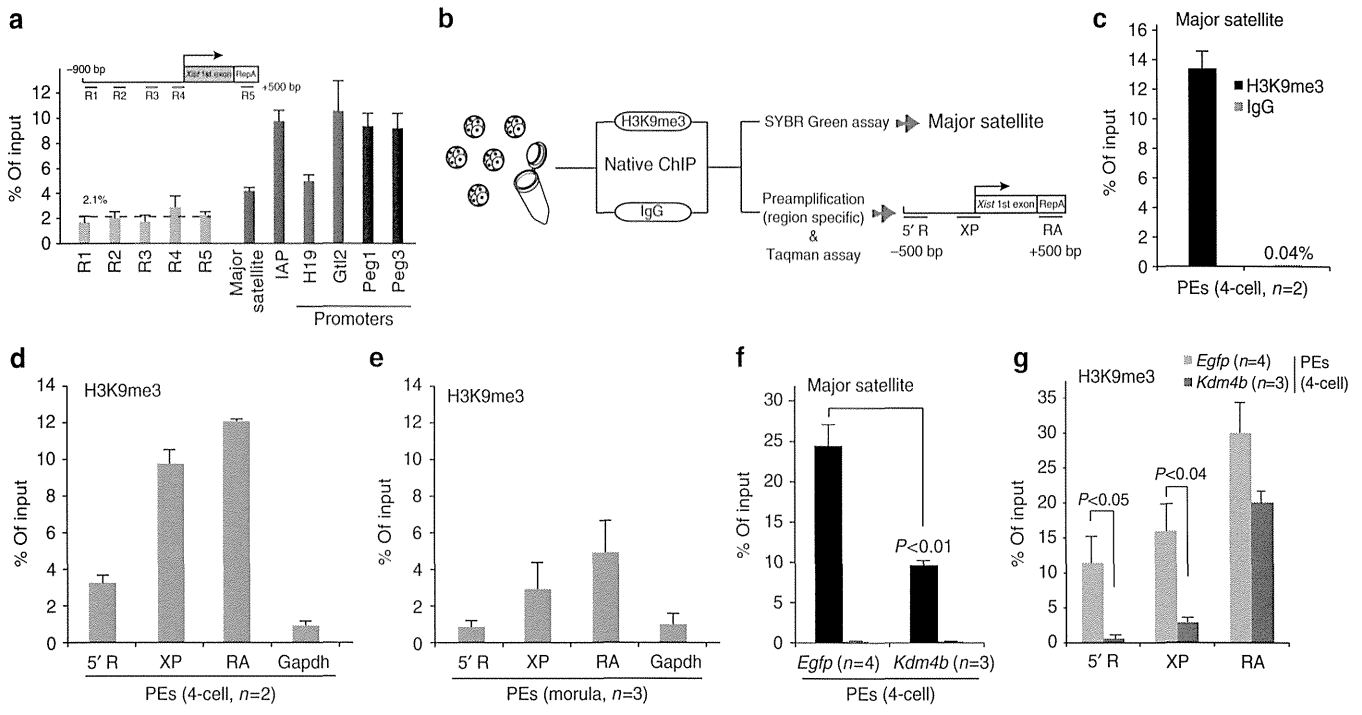

Figure 4 | H3K9me3 states at the Xm-*Xist* promoter region in preimplantation embryos. (**a**) ChIP-qPCR analysis of Xp (sperm) at *Xist* 5′-regions, the *H19*, *Gtl2*, *Peg1* and *Peg3* promoter region, and regions in repetitive elements. $n=2$–4. Rabbit IgG was used as a negative control. The percentage of input for negative control DNA was >1% for all genes tested. The data were not normalized for local nucleosome occupancies. (**b**) Schematic representation of eChIP-qPCR analysis. H3K9me3 states at major satellite regions (**c**) and at *Xist* regions and the *Gapdh* promoter region (**d**) in PEs at the four-cell stage. Two independent experiments were performed. In each experiment, 250 embryos were used. (**e**) H3K9me3 states at the *Xist* and *Gapdh* promoter regions in morula-stage embryos. Three independent experiments were conducted and 40 embryos were used for each assay. H3K9me3 states in major satellite (**f**) and *Xist* regions (**g**) in *Egfp*- and *Kdm4b*-PEs at the four-cell stage. Three (*Kdm4b*-PEs) and four (*Egfp*-PEs) independent experiments were conducted. In each experiment, 170–250 embryos were prepared. The percentages of input for negative controls (IgG) were <0.2% (**f**) and 1.9% (**g**), respectively. Error bars indicate the mean ± s.e.m. The *P*-values were determined using Student's *t*-tests.

Next, we examined whether Xm-*Xist* derepression from the four-cell stage by ectopic *Kdm4b* expression or TSA treatment was regulated by RNF12 (Supplementary Fig. 6d). Four-cell embryos of *Kdm4b*- or *Egfp* + TSA-PEs treated with si-Rnf12 were analysed by qPCR. Depletion of RNF12 did not affect Xm-*Xist* expression in *Egfp* + TSA-PEs compared with the si-control PEs (Fig. 3e), suggesting that factors other than RNF12 may contribute to histone acetylation-mediated Xm-*Xist* activation. This observation is consistent with results obtained using *Rnf12*$^{-/-}$ mice, which demonstrated that *Xist* is activated by RNF12 and other unidentified factors[5,22]. In contrast, *Xist* expression in *Kdm4b*-PEs derived from oocytes treated with si-*Rnf12* did not induce detectable expression of Xm-*Xist* (Fig. 3f). These results demonstrated that KDM4B-mediated Xm-*Xist* expression depended on RNF12 and suggested that H3K9me3 prevented the expression.

Promoter demethylation of H3K9me3 causes Xm-*Xist* derepression. As activation of *Xist* by RNF12 is essential for establishing iXCI[5], we attempted to determine the mechanism responsible for the transcriptional derepression of Xm-*Xist* by KDM4B-mediated demethylation of H3K9me3. We first examined whether H3K9me3 levels were enriched at the Xp-*Xist* promoter region. Nucleosomes were extracted from the sperm genome (Supplementary Fig. 7). ChIP-qPCR revealed the low H3K9me3 levels of Xp-*Xist* in the 5′-regions containing the major promoter for *Xist* expression (average: 2.1%; Fig. 4a), as compared with those of the *H19*, *Gtl2*, *Peg1* and *Peg3* promoter loci (average: 8.5%) and regions in repetitive elements (intracisternal A-particles and major satellite DNAs; average: 7.0%), which are known to be associated with H3K9me3 (ref. 23). These results indicated that the *Xist* promoter region was hypomethylated in sperm, in agreement with Xp-*Xist* being expressed in early embryogenesis.

Preparing sufficient numbers of embryos or oocytes for ChIP combined with deep sequencing (ChIP-seq) analysis is problematic. Some ChIP-qPCR methods requiring small samples have been reported[24]; however, most of these studies are based on a cross-linking ChIP method, in which the ChIP efficiency is lower than that of native ChIP methods[25]. Thus, we developed a new native ChIP method combined with a Taqman qPCR system for quantification of transcription in single cells (termed eChIP-qPCR) and focused on three loci at *Xist* 5′-regions containing the major promoter and repeat A, which is essential for establishment of iXCI[26] (Fig. 4b). We first tested whether the quantification system was biased by using diluted DNA from bulk ES cells. The results of ChIP-qPCR from pre-amplified DNA were comparable to those obtained without pre-amplification (Supplementary Fig. 8).

Using this system, we examined H3K9me3 states at three *Xist* regions and at *Gapdh* promoter regions (as a negative control) in PEs at the four-cell stage. We first investigated whether our eChIP method was efficient by examining major satellite repeats that have been identified as H3K9me3-rich regions in preimplantation embryos[23]. Consistent with a previous report, H3K9me3 was highly enriched at major satellite regions (Fig. 4c). The three *Xist* regions were also highly methylated compared with the *Gapdh* promoter region, as follows: 5′-R, 3.7-fold upregulated; XP, 9.8-fold upregulated; RA, 12.1-fold upregulated; (Fig. 4d).

As Fig. 2a showed Xm-*Xist* spontaneous derepression at the morula stage, we next investigated whether H3K9me3 levels at the *Xist* promoter region were low at this stage. eChIP-aPCR

analysis revealed that enrichment of H3K9me3 was markedly reduced compared with that at the *Gapdh* promoter region in the four-cell stage (5′-R, 0.83-fold upregulated; XP, 2.85-fold upregulated; RA, 4.8-fold upregulated; Fig. 4e). These results suggested that demethylation at the promoter region was essential for Xm-*Xist* derepression.

We then asked whether *Xist* promoter demethylation was involved in the Xm-*Xist* derepression observed in *Kdm4b*-PEs at the four-cell stage. The H3K9me3 levels at major satellite regions in *Kdm4b*-PEs were significantly reduced compared with those in *Egfp*-PEs (*Kdm4b*-PEs: 9.74% versus *Egfp*-PEs: 24.63%, $P<0.01$, Student's *t*-tests; Fig. 4f). At three *Xist* regions, the H3K9me3

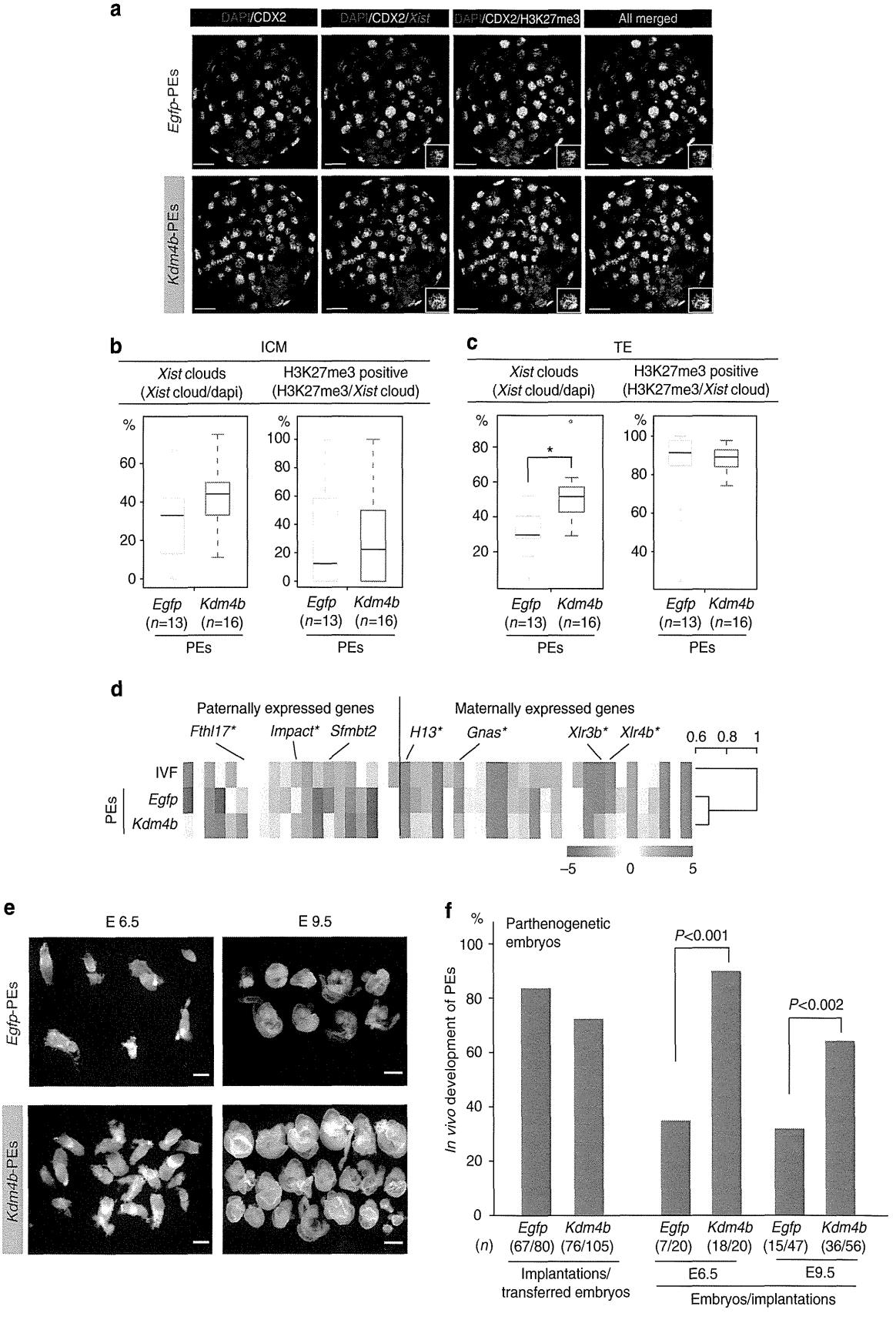

Figure 5